JOURNAL OF GEOPHYSICAL RESEARCH, VOL. 116, F03023, doi:10.1029/2010JF001941, 2011

Quantifying the forcing effect of channel width variations on free bars: Morphodynamic modeling based on characteristic dissipative Galerkin scheme

Fu-Chun Wu,[1,2] Yun-Chuan Shao,[1] and Yu-Chen Chen[1]

Received 1 December 2010; revised 9 June 2011; accepted 22 June 2011; published 15 September 2011.

[1] The forcing effect of channel width variations on free bars is investigated in this study using a two-dimensional depth-averaged morphodynamic model. The novel feature of the model is the incorporation of a characteristic dissipative Galerkin (CDG) upwinding scheme in the bed evolution module. A correction for the secondary flows induced by streamline curvature is also included, allowing for simulations of bar growth and migration in channels with width variations beyond the small-amplitude regimes. The model is tested against a variety of experimental data ranging from purely forced and free bars to coexisting bed forms in the variable-width channel. The CDG scheme effectively dissipates local bed oscillations, thus sustains numerical stabilities. The results show that the global effect of width variations on bar height is invariably suppressive. Such effect increases with the dimensionless amplitude A_C and wave number λ_C of width variations. For small A_C, λ_C has little effects on bar height; for A_C beyond small amplitudes, however, the suppressing effect depends on both A_C and λ_C. The suppressing effect on bar length increases also with both A_C and λ_C, but is much weaker than that on bar height. The global effect of width variations on bar celerity can be suppressive or enhancive, depending on the combination of A_C and λ_C. For smaller λ_C, the effect on bar celerity is enhancive; for larger λ_C, bar celerity tends to increase at small A_C but decreases for A_C beyond small amplitudes. We present herein an unprecedented data set verifying the theoretical prediction on celerity enhancement. Full suppression of bar growth above the theoretically predicted threshold A_C was not observed, regardless of the adopted amplitude of initial bed perturbation A. The global effects of width variations on free bars can be quantified using a forcing factor F_C that integrates the effects of A_C and λ_C. The suppressing effects on bar height and length are both proportional to $F_C^{2.16}$; the global effect on bar celerity is, however, a parabolic function of F_C.

Citation: Wu, F.-C., Y.-C. Shao, and Y.-C. Chen (2011), Quantifying the forcing effect of channel width variations on free bars: Morphodynamic modeling based on characteristic dissipative Galerkin scheme, *J. Geophys. Res.*, *116*, F03023, doi:10.1029/2010JF001941.

1. Introduction

[2] Bars are large-scale bed forms observed in rivers, with their heights and lengths typically scaled with the flow depth and channel width, respectively. Two classes of bars, namely, free and forced bars are distinguished according to their origins and morphological features [*Seminara and Tubino*, 1989]. Free bars arise from an inherent instability of erodible beds subject to turbulent flows [*Callander*, 1969; *Colombini et al.*, 1987; *Tubino et al.*, 1999], where the growth of bed perturbations leads to the spontaneous development of migrating alternate bars in straight channels. Free bars are characterized by the alternating sequence of riffles and pools separated by sharp diagonal fronts. The wavelengths of alternate bars are ~8 to 10 channel widths, and the maximum bar heights are ~1 to 2 flow depths [*Whiting and Dietrich*, 1993; *Garcia and Nino*, 1993; *Lanzoni*, 2000a]. Once fully developed, the alternate bars maintain their morphology while migrating downstream, as revealed by the steady translation of bar fronts.

[3] Forced bars, on the other hand, are stationary bed deformations arising from the forcing effects of spatial non-uniformity, such as channel curvature or width variations. A typical example of curvature-induced bed forms is the point bars established at the inner bends of a meandering channel [*Ikeda and Parker*, 1989], where the alternating bar configuration arises as a result of the asymmetric forcing associated with the periodic change of sign of channel curvature. In contrast, central bars and two-side bars are symmetric bed deformations developed at the wide sections of a variable-width channel [*Bittner*, 1994; *Repetto and Tubino*, 2001; *Wu and Yeh*, 2005], where the transverse structure of the forced

[1]Department of Bioenvironmental Systems Engineering, National Taiwan University, Taipei, Taiwan.
[2]Hydrotech Research Institute, National Taiwan University, Taipei, Taiwan.

Copyright 2011 by the American Geophysical Union.
0148-0227/11/2010JF001941

bed forms arises as a consequence of the symmetric forcing induced by streamline convergence-divergence associated with the periodic width variations. The irregular bed topographies observed in natural streams may consist of a decipherable mixture of free and forced bars [*Furbish et al.*, 1998].

[4] It has been observed in the fields and laboratory flumes that when the forcing effects are sufficiently strong, the migrating alternate bars are suppressed in favor of the development of forced bed topographies. Coexistence of free and forced bars in weakly curved channels and transition from migrating alternate bars to stationary point bars in developing meanders have been extensively investigated through flume studies [*Kinoshita and Miwa*, 1974; *Gottlieb*, 1976; *Fujita and Muramoto*, 1982, 1985]. *Kinoshita and Miwa* [1974] first observed the existence of a threshold value of channel curvature above which bar migration is suppressed, which was later analytically interpreted by *Tubino and Seminara* [1990]. The experimental results of *Garcia and Nino* [1993] indicated that the channel curvature in general tends to damp the height of alternate bars and slow down their migration. Further experiments performed by *Whiting and Dietrich* [1993] revealed that the migrating alternate bars would temporarily stall when in phase with the point bars, leading to a reduced bar celerity compared to that observed in a straight channel, which confirms the numerical prediction made by *Shimizu and Itakura* [1989]. These results may have practical implications. An example is that stream restoration work aimed at stabilizing the streambed can specify a slightly sinuous alignment to promote suppression of migrating bed features [*Seminara*, 2006].

[5] In contrast to the much studied phenomenon of coexisting free and forced bed forms in the meandering channels, the coexistence of free and forced bars in the variable-width channels and their nonlinear interactions received attention only recently [*Bittner*, 1994; *Repetto and Tubino*, 1999; *Repetto*, 2000; *Wu and Yeh*, 2005]. *Repetto and Tubino* [1999] presented an analysis based on a weakly nonlinear approach (in terms of the forcing effect) and a linear stability theory (in terms of the bar growth) to ascertain the effect of periodic width variations on the development process of free bars. Their analysis relied on the assumption that the dimensionless amplitudes of width perturbation (A_C) and bed perturbation (A) are both small, with the latter being much smaller than the former, i.e., $A \ll A_C \ll 1$ [*Repetto*, 2000]. The output results of their analysis suggested that: (1) the effects of width variations on free bars are invariably suppressing; (2) the damping effects on free bars depend primarily on the amplitude of width variations, but are only slightly dependent upon the wave number of width variations; (3) a threshold amplitude of width variations exists, above which free bars are fully suppressed; (4) width variations in general slow down the migration of alternate bars, however, very slow spatial variations of channel width (i.e., very small wave numbers) may speed up bar propagation. The experimental results of *Repetto and Tubino* [1999] revealed that the leading Fourier components of bed topography obtained in the variable-width channels exhibit a suppressed alternate bar mode but enhanced longitudinal and transverse modes of forced bed topography as compared to those measured in the straight channels. Experimental studies performed with increasing amplitudes of width variations further confirmed the predicted full suppression of alternate bars above the threshold conditions [*Bittner*, 1994; *Bolla Pittaluga et al.*, 2001; *Repetto et al.*, 2002]. It was also demonstrated that, due to the interactions between free and forced bed responses, the heights and wavelengths of alternate bars observed in the variable-width channels are consistently smaller than those observed in their straight counterparts [*Lanzoni and Tubino*, 2000].

[6] Despite the above mentioned experimental studies that have been conducted to verify the theoretical predictions, several unresolved questions remain to be asked. (1) Do the variations of channel width invariably suppress free bars? Specifically, could very small wave numbers of width variations speed up bar migration as predicted by the linear stability theory? This has never been confirmed experimentally or numerically. (2) Is the effect of width variations on free bars invariably less dependent on the wave number of width variations than on the amplitude of width variations? (3) What would happen if the small-amplitude assumptions for the width variations and bed perturbation are violated? Specifically, would the growth of free bars be fully suppressed by the amplitude of width variations that is above the predicted threshold if the bed perturbation is beyond the small-amplitude regime? (4) An extended but probably more important question to ask: Would it be possible to combine the amplitude and wave number of width perturbations as a single, integrated factor that can be used to quantify the overall forcing effect of width variations on free bars?

[7] In this paper we aim to answer these questions using a numerical simulation approach. The numerical model to be used for the task should be able to handle the case of free bar migration in channels with periodic width variations, where nonlinear interactions take place between the free and forced bed responses. To this aim, we develop a finite element (FE) model suitable for the convection-dominated morphodynamic system, based on the characteristic dissipative Galerkin (CDG) spatial discretization of the hydrodynamic equations and sediment continuity equation, the latter is a novel contribution of this study. The proposed model allows a fully nonlinear study of the interactions between free and forced bed responses beyond the small-perturbation regimes. The key features of numerical modeling essential for the present study are summarized below.

2. Numerical Modeling

[8] Before we start to formulate our numerical model, a brief review of the available models most relevant to the present study is helpful. For alluvial channels with nonerodible banks, a morphodynamic model solves the hydrodynamic equations and sediment continuity equation to simulate the evolution of bed topography caused by erosion and deposition of sediment. The hydrodynamic equations, which include continuity and momentum equations of water flow, are a system of hyperbolic partial differential equations (PDEs), and the sediment continuity (or Exner) equation is also a hyperbolic PDE. The hyperbolic PDE physically describes two mechanisms of transport, i.e., convection and diffusion [*Jansen et al.*, 1979], also referred to as translation and dispersion [*Lisle et al.*, 2001]. In some cases, one of the mechanisms may dominate over the other. For example, the Exner equation may be reduced to a parabolic PDE, or

diffusion equation, to model bed aggradation and degradation induced by the change of sediment supply [*Gill*, 1987]. In contrast, for channels with migrating bed forms, such as free alternate bars whose convective nature has been demonstrated analytically [*Federici and Seminara*, 2003], the hyperbolic version of the Exner equation has to be used.

[9] Computationally, the hydrodynamic and Exner equations may be solved using a coupled or decoupled approach. In a fully coupled approach the hydrodynamic and Exner equations are solved simultaneously, whereas in a decoupled (or semi-coupled) approach the Exner equation is solved after the hydrodynamic equations. For most river applications where the morphodynamic time scale is much greater than the hydraulic time scale, the flowfield may well be approximated as quasi-steady [*de Vries*, 1965], thus the use of a decoupled approach is appropriate where the specified bed topography remains fixed during each time step of hydraulic computation and then with the solved flowfield the bed topography is updated via the Exner equation. Although the coupled three-dimensional (3D) morphodynamic modeling is recently made possible due to the advances in computational power [e.g., *Chou and Fringer*, 2010], the extremely high cost of the coupled 3D computation makes the decoupled two-dimensional (2D) model a preferred choice for most practical applications.

[10] The finite element method (FEM) has been an attractive tool for morphodynamic modeling, primarily due to its flexibility to adapt to complicated planform geometries and natural boundary conditions. The conventional Galerkin FEM (GFEM) is a centered scheme appropriate for the diffusive problems. Applying the GFEM to the convection-dominated systems often introduces spurious oscillations in the vicinity of discontinuities leading to severe numerical instabilities [*Donea and Huerta*, 2003]. The river morphology model River2D-MOR recently presented by *Vasquez et al.* [2007] was built by semi-coupling the Exner equation with the existing depth-averaged 2D FE hydrodynamic model River2D [*Steffler and Blackburn*, 2002]. In the River2D model a characteristic dissipative Galerkin (CDG) scheme [*Hicks and Steffler*, 1992] is employed to solve the hyperbolic system of hydrodynamic equations where the convective transport dominates. The CDG scheme is a streamline upwind Petrov-Galerkin (SUPG) scheme [*Brooks and Hughes*, 1982] in which the upwind weighted test functions are used to introduce selective dissipation of spurious oscillations based on the characteristic velocities of both progressive and regressive disturbances. *Hicks and Steffler* [1995] compared three FE schemes specifically designed for the hyperbolic systems, and concluded that the CDG scheme outperforms the others because of the balanced treatment of both disturbance components and little sensitivity to parameter variations. However, to date the CDG scheme has only been applied in the discretization of hydrodynamic equations but has never been applied in the bed evolution module for discretization of the Exner equation, thus the River2D-MOR model is not suitable for the convective problems such as migrating bed forms. Moreover, when applied to simulate the formation of forced bars in the variable-width channels [*Vasquez*, 2005; *Vasquez et al.*, 2007], some stability problems caused by the acute local changes in bed elevation at the corners along sidewalls prevented the application of the River2D-MOR model to its full extent. Lately a simplest first-order upwinding scheme has been incorporated into the bed evolution module of the River2D-MOR model [*Kwan*, 2009], such a scheme would, however, introduce severe numerical diffusion into the solution where large gradients exist [*Patankar*, 1980].

[11] To simulate the growth of free bars in straight channels, a number of numerical studies have been conducted. For example, *Nelson and Smith* [1989] and *Nelson* [1990] presented a 2D model combining the fully nonlinear flow equations, sediment transport and bed evolution calculations. Their results indicated that the initial instability of alternate bars is a simple topographic steering response, while the eventual finite-amplitude stability of free bars results from a balance between topographic steering, gravitational effect induced by bar slopes, and secondary flows associated with streamline curvature. *Federici and Seminara* [2003] built a 2D finite difference (FD) model by semi-coupling the Exner equation with the shallow water equations. Their simulation results demonstrated that (1) starting from either a randomly distributed or localized bed perturbation, the alternate bar trains would grow and migrate downstream leaving the source area undisturbed; (2) the persistent pattern of alternate bars observed in the laboratory flumes arises from some persistent initial perturbations; (3) the nonlinear development of such perturbations leads to an equilibrium bar pattern with its amplitude independent of the amplitude of the initial perturbation whereas the distance needed to achieve equilibrium reduces with increasing amplitude of initial perturbation. *Bernini et al.* [2006] investigated the gravitational effect of transverse bed slope on the equilibrium bar characteristics using a 2D FD model semi-coupling the Exner equation with the shallow water equations. *Defina* [2003] developed a decoupled 2D FE model to simulate the growth of free bars in straight channels and tested against the experimental data from *Lanzoni* [2000a]. Using four types of initial bed disturbance to trigger bar formation, *Defina* [2003] found that the initial stages of development and the equilibrium bar characteristics are strongly affected by the way bars are generated. Nevertheless, the relations between equilibrium bar height, bar length and celerity collapse on single curves regardless of the type of initial bed disturbance. The implication of these results for the current study is that a consistent way of initial bed disturbance should be employed to trigger bar formation, such that the equilibrium bar characteristics can be compared on a common ground.

[12] We use in this study the FE method because of its geometric flexibilities better suited for complex planforms. Currently, the available FE morphodynamic models lack a robust upwinding scheme for discretization of the Exner equation. As a result, these FE models would end up with numerical instabilities or degraded flow/bed variables when applied to the convection-dominated problems [*Oden and Carey*, 1983]. Hence, there is a pressing need for a morphodynamic model that is applicable to simulations of bar growth and migration in variable-width channels.

[13] The morphodynamic model presented in this paper is based on the CDG discretization of the hydrodynamic and Exner equations. The model is applicable to the hyperbolic systems where convective transport of flow and bed form prevails. The model integrates a hydrodynamic module and a bed evolution module in a semi-coupled fashion. The hydrodynamic module is constructed following closely the

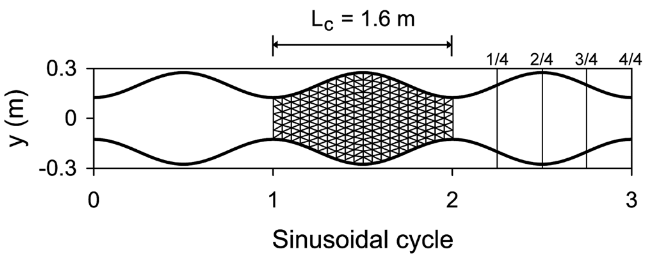

Figure 1. Variable-width channel used in run C1–11 [*Bittner*, 1994]. The channel consists of eight sinusoidal cycles; three are shown here with structured triangular FE mesh depicted in one of them. Mean channel width $2B_0$ = 0.4 m; amplitude and wavelength of width variations A_CB_0 = 0.075 m and L_C = 1.6 m; mean element sizes Δx = 0.08 m and Δy = 0.045 m. Labeled with 1/4~4/4 are the four cross sections of a sinusoidal cycle whose transverse profiles of equilibrium bed deformation and flow depth are shown in Figures 3 and 4.

CDG-based depth-averaged 2D FE model developed by *Steffler* [1997], while the bed evolution module is a novel contribution because the CDG scheme has never been implemented on the Exner equation. Details of model formulation are described in Appendix A.

3. Model Test

[14] The proposed CDG-based morphodynamic model is tested in this section against a variety of experimental data. The first is the purely forced bars observed in the variable-width channels. Two data sets are used: one is the two-side bars from *Bittner* [1994]; the other is the central bars from *Wu and Yeh* [2005]. The second is the migrating alternate bars in the constant-width straight channel. A data set from *Lanzoni* [2000a] is used. The third is coexisting free and forced bars in the variable-width channel from *Wu and Yeh* [2005]. The details of the experimental conditions, model setting, and results comparison are described below.

3.1. Forced Bars in Variable-Width Channels

3.1.1. Two-Side Bars

[15] The experimental data from run C1–11 of *Bittner* [1994] are used to verify the formation of two-side bars in the variable-width channel. The experiment was performed in a channel with sinusoidal width variations, which are described by

$$B(x) = B_0[1 + A_C \sin(2\pi x/L_C)] = B_0[1 + A_C \sin(\lambda_C x/B_0)] \quad (1)$$

where $B(x)$ = channel half-width at x; B_0 = mean half-width of the channel; L_C = wavelength of width variation; A_C = dimensionless amplitude of width variation; λ_C = dimensionless wave number of width variation = $2\pi B_0/L_C$. The parameters of the channel used in run C1–11 are B_0 = 0.2 m, A_C = 0.375, L_C = 1.6 m, and λ_C = 0.785. The channel consists of eight sinusoidal cycles; three of them are shown in Figure 1. The unit discharge q_{in} = 7.3 × 10^{-3} m^2/s, channel slope S_0 = 0.004, bed material is well-sorted sand with d_s = 0.53 mm. The experiment was run for >6 h; the final equilibrium bed topography and flow depth were measured in the mid four cycles. The mean flow depth h_0 = 2.2 cm, which gives a Shields stress for the reference uniform flow θ_0 = 0.102.

[16] The computational domain includes a total of eight sinusoidal cycles, with the upstream and downstream ends extended with constant-width (= $2B_0$) fixed-bed reaches. Uniform flows are specified in the extended reaches, with the inflow bed load transport rate $q_{b,in}$ = 5.07 × 10^{-6} m^2/s evaluated from the given θ_0. These extended fixed-bed reaches ensure that an equilibrium bed configuration eventually develops in the variable-width reach [*Defina*, 2003]. The numerical simulation was run for a sufficient time to ensure that an equilibrium stage was reached. Also shown in Figure 1 is the structured triangular FE mesh in one of the cycles. A total of 3,200 elements with 1,768 nodes are included in the entire computational domain, with mean element sizes Δx = 0.08 m and Δy = 0.045 m.

[17] The simulated equilibrium bed topography is shown in Figure 2, where the measured bed topography and the linear solution from *Wu and Yeh* [2005] are also shown for a comparison. The numerical result is generally in satisfactory agreement with the measured data. The observed longitudinal patterns of deposition at the wide sections and scour at the narrow ones, and formation of two-side bars at the wide sections are well captured by the numerical model. To further demonstrate this, the transverse profiles of equilibrium bed deformation at the four cross sections of a sinusoidal cycle (see Figure 1) are shown in Figure 3, along with the cycle-averaged data and the linear solution. The transverse bed profiles are, in general, well reproduced by the numerical model. At the wide section (2/4 cycle), the numerical result slightly underestimates deposition at the bar crests, while the linear solution tends to overestimate deposition particularly at the center. At the narrow section (4/4 cycle) and transitional sections (1/4 and 3/4 cycles), both the numerical result and linear solution coincide reasonably well with the observed

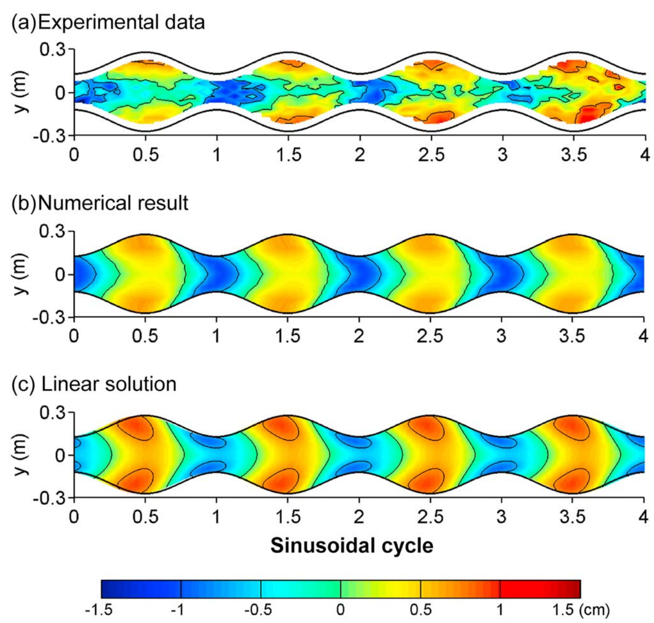

Figure 2. Equilibrium bed deformation of run C1–11: (a) Observed two-side bars [*Bittner*, 1994]; (b) numerical result (this study); (c) linear solution [*Wu and Yeh*, 2005].

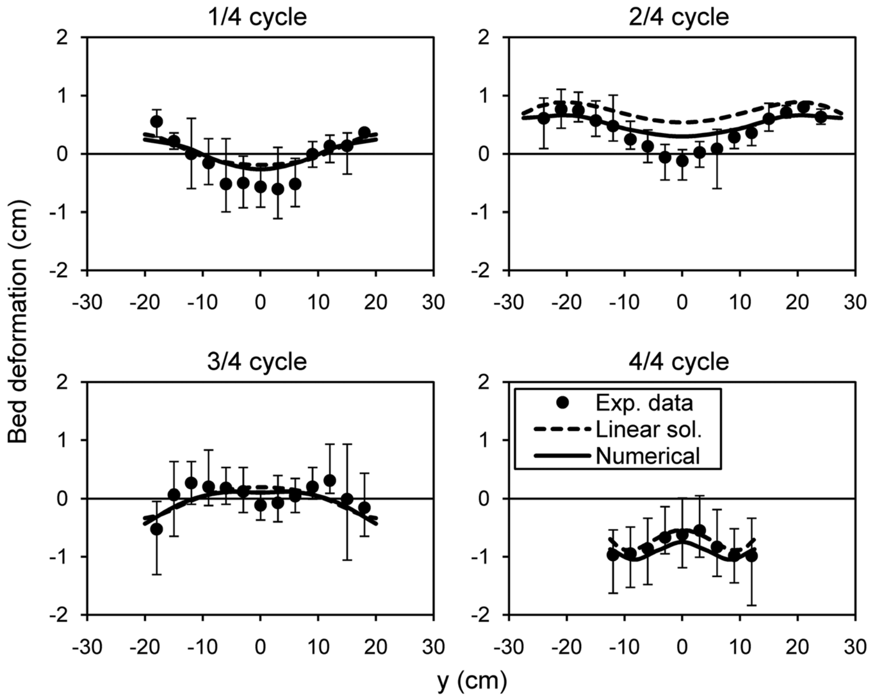

Figure 3. Transverse profiles of equilibrium bed deformation at four cross sections (see Figure 1) of a sinusoidal cycle (run C1–11). The cycle-averaged data [*Bittner*, 1994], numerical result (this study), and linear solution [*Wu and Yeh*, 2005] are shown for a comparison.

bed profiles. Because of the correction for the secondary flows induced by streamline curvature in the direction of bed shear stress that is incorporated in the numerical model and linear solution [*Wu and Yeh*, 2005], they both provide a satisfactory approximation to the observed bed topography. Such correction is particularly important when the small-amplitude assumption for width variations is relaxed. In this case the numerical result outperforms the linear solution probably because the value of A_C (= 0.375) is way beyond the small-amplitude assumption upon which the linear solution is based.

[18] To further test the hydrodynamic module, the transverse distributions of equilibrium flow depth at the four cross sections of a sinusoidal cycle (Figure 1) are shown in Figure 4, along with the cycle-averaged data and the linear solution. Generally, the numerical result correctly reflects the variations of flow depth. Longitudinally, the smaller depth at the wide section (2/4 cycle) and greater depth at the narrow section (4/4 cycle) are well captured. Transversely, the concave and convex profiles are satisfactorily reproduced. However, at the wide section, both the numerical and linear solutions tend to underestimate flow depth near the center; while at the narrow section, both solutions underestimate flow depth near the walls. This result is possibly related to the neglecting of secondary circulations due to topographic steering in the hydrodynamic equations.

[19] It should be noted here that the stability problem encountered by the previous investigators [*Vasquez*, 2005; *Vasquez et al.*, 2007] did not arise during our numerical simulations. It has been reported that the acute local bed perturbations are induced by the extreme nodal velocities at the corners where rapid changes in flow direction take place. The extreme nodal velocities would not affect the stability of the hydrodynamic module but have a strong influence on the bed evolution module because such local bed perturbations tend to grow and propagate, and eventually turn the model unstable. By incorporating the CDG scheme in the bed evolution module, we were able to dissipate such perturbations and sustain the stability of the morphodynamic simulation.

3.1.2. Central Bars

[20] The experimental data from run S-6 of *Wu and Yeh* [2005] are used to verify the formation of central bars in the channel with a much smaller value of λ_C (= 0.3). The channel, 10 m long, consists of three sinusoidal cycles with A_C = 0.156, L_C = 3.35 m, and B_0 = 0.16 m, and is given the unit discharge q_{in} = 0.02 m^2/s, channel slope S_0 = 0.003, and well-sorted bed material with d_s = 1.58 mm. The experiment was run for >8 h; the final equilibrium bed topography in the mid two cycles was measured using a laser scanner. The mean flow depth h_0 = 4.49 cm yields a value of θ_0 = 0.052 for the reference uniform flow. The computational domain is lengthened to include a total of six sinusoidal cycles; the upstream and downstream ends are extended with the constant-width fixed-bed reaches, where uniform flows are imposed, with the bed load transport rate $q_{b,in}$ evaluated from the given value of θ_0. A total of 4,200 triangular elements and 2,457 nodes are included in the entire domain, with mean element sizes Δx = 0.067 m, Δy = 0.053 m.

[21] The computed equilibrium bed topography along with the measured data and linear solution from *Wu and Yeh* [2005] are shown in Figure 5, where satisfactory agreement between the computed and measured results is demonstrated. The longitudinal pattern with deposition at the wide sections and scour at the narrow ones, and formation of central bars at the wide sections are correctly reproduced. The transverse profiles of bed deformation at the wide and narrow sections

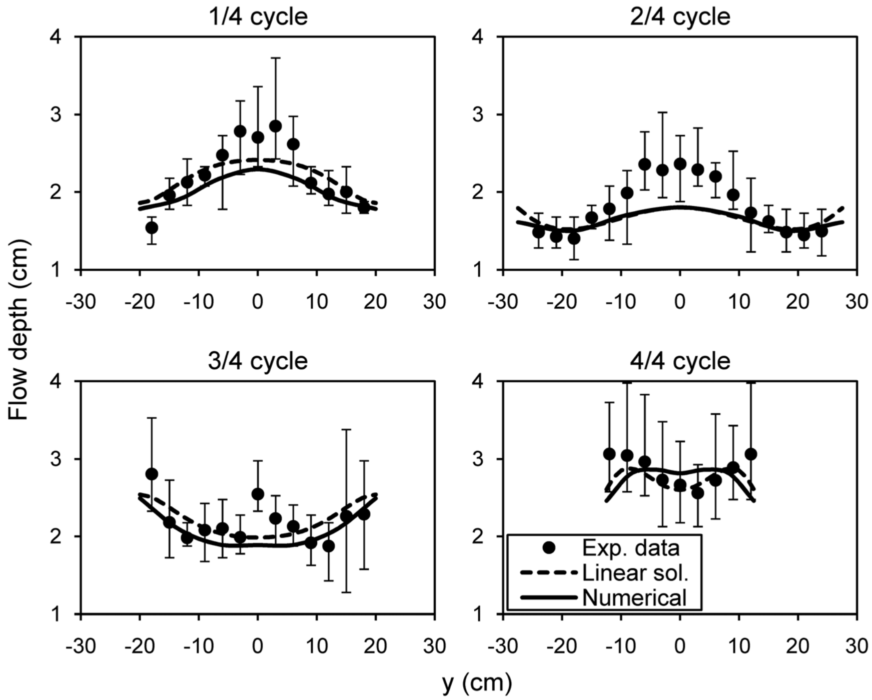

Figure 4. Transverse distributions of equilibrium flow depth at four cross sections (see Figure 1) of a sinusoidal cycle (run C1–11). The cycle-averaged data [*Bittner*, 1994], numerical result (this study), and linear solution [*Wu and Yeh*, 2005] are shown for a comparison.

are shown in Figure 6, along with the cycle-averaged data and the linear solution, where similar results are obtained with the numerical model and the linear solution. However, it is revealed that at the wide section, the near-wall deposition is over predicted, whereas at the narrow section, the near-wall scour is overestimated. The discrepancies in the near-wall bed topography are probably attributed to the fact that the 3D wall boundary layer effects are not accounted for in the 2D depth-averaged model, and also due to the local velocity distortion caused by the relaxed no-slip condition at the walls that becomes particularly significant at small values of λ_C, as previously elucidated by *Wu and Yeh* [2005]. Other simplifications made in this study, such as neglecting the effects of small bed forms, sloping bed, inertial lag, and topographic steering, may also contribute to the discrepancy between the computed and observed near-wall bed topographies.

3.2. Free Bars in Straight Channel

[22] Migration of free alternate bars is a convective propagation of bed forms. As noted earlier, a morphodynamic model based on the conventional Galerkin scheme is numerically unstable when applied to such a problem. To address this instability issue, previous investigators [*Defina*, 2003; *Vasquez*, 2005] employed degraded spatial resolutions for the bed load flux and bed deformation as an alternative solution strategy. The proposed CDG-based morphodynamic model is tested in this section against the experimental data from *Lanzoni* [2000a] to examine whether the growth of free bars can be reproduced without degrading the resolution of the bed evolution module.

[23] The test performed here follows the numerical experiments of *Defina* [2003] simulating the observed processes of bar growth in a straight channel [*Lanzoni*, 2000a]. The channel is 55 m long and 1.5 m wide; the bed material is well-sorted sand with d_s = 0.48 mm. The experimental conditions of run P1505 are adopted, which include the unit discharge q_{in} = 0.02 m^2/s, channel slope S_0 = 0.0045, normal depth h_0 = 0.044 m, and bed load transport rate $q_{b,in}$ = 1.13 × 10^{-5} m^2/s. A computational domain 100 m in length, much longer than the actual length of the channel, is used allowing

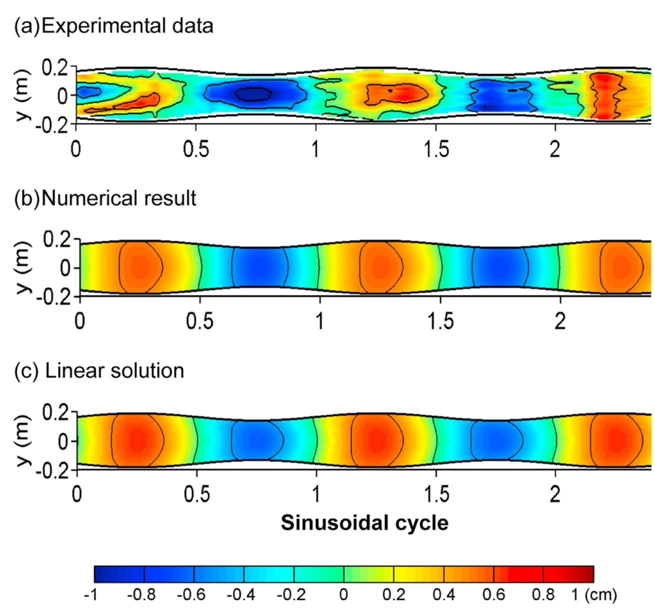

Figure 5. Equilibrium bed deformation of run S-6: (a) Observed central bars [*Wu and Yeh*, 2005]; (b) numerical result (this study); (c) linear solution [*Wu and Yeh*, 2005].

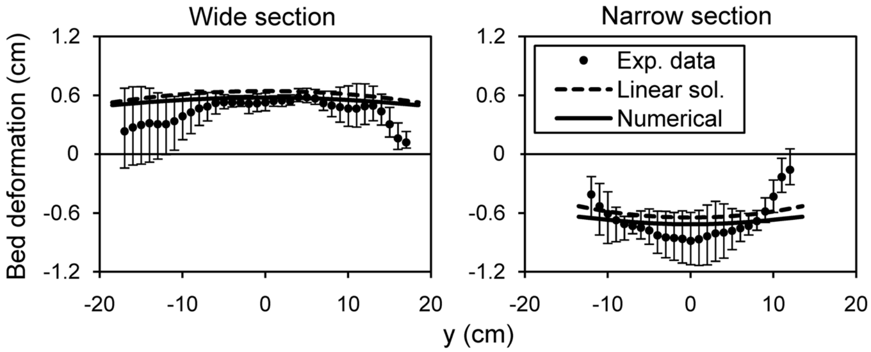

Figure 6. Transverse profiles of equilibrium bed deformation at wide and narrow sections of a sinusoidal cycle (run S-6). The cycle-averaged data [*Wu and Yeh*, 2005], numerical result (this study), and linear solution [*Wu and Yeh*, 2005] are shown for a comparison.

for the sufficient growth of free bars before they leave the domain [*Defina*, 2003]. The fixed-bed reaches extended in the upstream and downstream ends are imposed with uniform flows, leading to an equilibrium bed load transport. The computational domain comprises a total of 7,680 triangular elements and 4,329 nodes, with mean sizes $\Delta x = 0.25$ m and $\Delta y = 0.15$ m.

[24] The channel is initially flat bedded. Following the approach used by previous investigators, a localized bump is introduced at the upstream end triggering the formation of free bars [*Defina*, 2003; *Federici and Seminara*, 2003; *Bernini et al.*, 2006]. This bed perturbation has a sinusoidal structure in both the longitudinal and transverse directions, which is similar to the localized bed disturbance adopted by *Federici and Seminara* [2003] and is expressed by

$$\delta z_b(x, y) = A_b \sin(\pi x/L_b) \sin(-\pi y/2B_0) \quad (2)$$

where δz_b = bed perturbation; A_b = amplitude of bed perturbation; L_b = longitudinal length of bed perturbation. The localized bump stretches from $x = 0$ to L_b and $y = -B_0$ to B_0. The adopted values of $A_b = 4$ mm and $L_b = 3.5$ m are consistent with those used by *Defina* [2003], who found that a localized initial bump is unable to trigger a persisting train of bars as observed in the flume experiments. The persisting train of bars may arise from the spatiotemporal growth of some persistent, random perturbations [*Defina*, 2003; *Federici and Seminara*, 2003]. It should be noted here that because the real perturbations are not known, any given distribution of initial disturbances is subjected to a strong degree of arbitrariness. The single bump adopted here thus only serves as an agent for triggering the formation of alternate bars.

[25] The simulated evolution of bed topography following the introduction of an initial bump is depicted in Figure 7, where a small-amplitude bar takes form immediately downstream of the initial bump (1 h), followed by two alternate bars generated downstream. These newly formed bars, along with the initial bump, keep migrating while growing in their sizes, meanwhile trigger the formation of new bars further downstream (2–3 h). By the end of 4 h, the well-developed train of bars reaches the downstream end. As the bars grow they lengthen and decelerate, and the lee faces become steeper resulting in the signature diagonal fronts (4–5 h). Following the first 2 h of rapid development, the growth of free bars gradually slows down. At the end of 7 h, several bars immediately downstream of the initial bump reach a quasi-equilibrium state while some new, further downstream bars have moved out of the domain. After the passage of the train of bars, the source area is left undisturbed, demonstrating fully the convective nature of free bars [*Defina*, 2003; *Federici and Seminara*, 2003; *Bernini et al.*, 2006]. The processes of bar growth demonstrated by our simulation results are faster than those reported by *Defina* [2003], but are more consistent with the observed results [*Lanzoni*, 2000a], which is probably attributable to the adopted initial bump that is more effective in triggering bar formation.

[26] The longitudinal profile of local bar height, defined as the difference in extreme elevations between the right- and left-half cross section, for the two bars located within x = 70 ~ 90 m (7 h) is compared to the observed result from *Lanzoni* [2000a], shown in Figure 8, where satisfactory agreement between the computed and observed results is demonstrated. The maximum bar height obtained from the simulation result is ~6 cm, close to the reported value of 7 cm. The simulated result of bar wavelength is ~11 m, also close to the reported value of 10 m. The computed result of bar celerity is ~4 m/h, greater than the reported value of 2.8 m/h but much more realistic than the value of 8.5 m/h predicted by the linear theory [*Lanzoni*, 2000a].

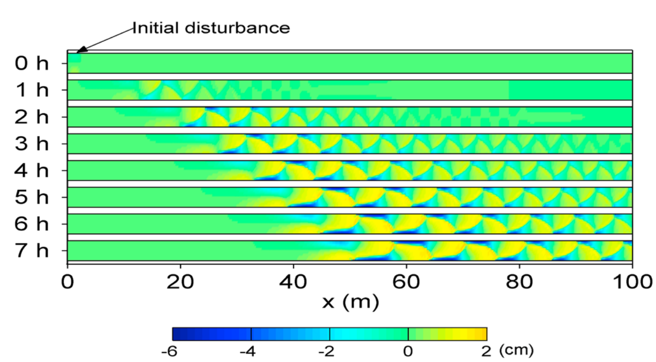

Figure 7. Simulation of bar evolution (bed deformation) following the introduction of an initial bed disturbance. As the alternate bars grow they lengthen and decelerate; the lee faces become steeper, leading to the signature diagonal fronts. After the passage of the train of bars, the source area is left undisturbed.

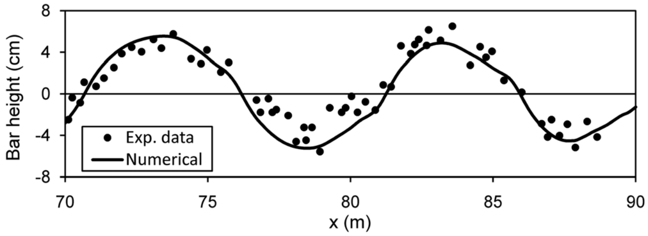

Figure 8. Longitudinal profile of local bar height (defined as the difference in extreme elevation between the right- and left-half cross section). Two bars located within x = 70 m ~ 90 m (7 h in Figure 7) are compared to the experimental data [*Lanzoni*, 2000a].

[27] So far we have tested the CDG-based morphodynamic model against the experimental data of purely forced bars developed in variable-width channels and growth of free bars in the straight channel. These results reveal that the proposed CDG-based model well captures the longitudinal and transverse topographic features associated with the complex planform. The proposed model also reproduces successfully the migrating bed forms while securing the numerical stability and spatial resolution. In the following section we further test the CDG-based model against a mixed case where forced and free bed forms coexist in a variable-width channel.

3.3. Coexisting Forced and Free Bars in Variable-Width Channel

[28] To be effectively used as a tool for investigating the nonlinear interactions of forced and free bed forms, the CDG-based model is further tested against the experimental data from run F-2 of *Wu and Yeh* [2005], where steady central bars and quasi-stationary alternate bars coexisted in a variable-width channel. The channel and sediment used in run F-2 and the FE mesh used for the computation are the same as those earlier used for run S-6 (see section 3.1.2). The experimental conditions include q_{in} = 0.0137 m^2/s, S_0 = 0.005, h_0 = 3.13 cm, and $q_{b,in}$ = 3.35 × 10^{-6} m^2/s. The equilibrium bed topography observed at the end of 9 h is shown in Figure 9a, where a distorted central bar is demonstrated.

[29] To simulate coexisting forced and free bars, a two-stage procedure is adopted. At the first stage, the model simulation is run for a sufficient time without introducing any disturbance such that an equilibrium forced bed form is developed (Figure 9c). At the second stage an upstream bed perturbation, described by (2) with A_b = 4 mm and L_b = 3.5 m, is introduced triggering the formation of alternate bars in the presence of forced bars. As mentioned earlier, because the real distribution of bed perturbations is not known, the localized bump used here is solely aimed to obtain the best possible result (Figure 9b) that is in agreement with the observed bed topography (Figure 9a). Following *Whiting and Dietrich* [1993], we subtract the forced component (Figure 9c) from the mixed bed forms (Figure 9b) to extract the free component, as shown in Figure 9d, where the alternate bars developed in the variable-width channel have a maximum amplitude of ~0.2 cm, smaller than the coexisting central bars whose amplitude is about twice that magnitude.

[30] To further compare the numerical and experimental results, the transverse profiles of bed deformation at the four cross sections of a sinusoidal cycle are shown in Figure 10, where the asymmetric profiles of scour and deposition respectively at the narrow section (1/4 cycle) and the wide section (3/4 cycle) are well captured by the numerical model, whereas at the transitional sections the scour (2/4 cycle) and deposition (4/4 cycle) are slightly underestimated. Overall, the CDG-based model reproduces with reasonable success the coexisting forced and free bars in the variable-width channel, thus confirming the effectiveness of the proposed model.

4. Effects of Width Variations on Free Bars

4.1. Numerical Experiments

[31] To study the effects of width variations on free bars, a series of numerical experiments are conducted using different combinations of channel parameters. The equilibrium characteristics of bars (i.e., bar height, length, and celerity) developed in the variable-width channels are compared to those developed in the reference straight channel, whose width $2B_0$ is the mean width of the variable-width channel. We use the parameter values adopted by *Bernini et al.* [2006]

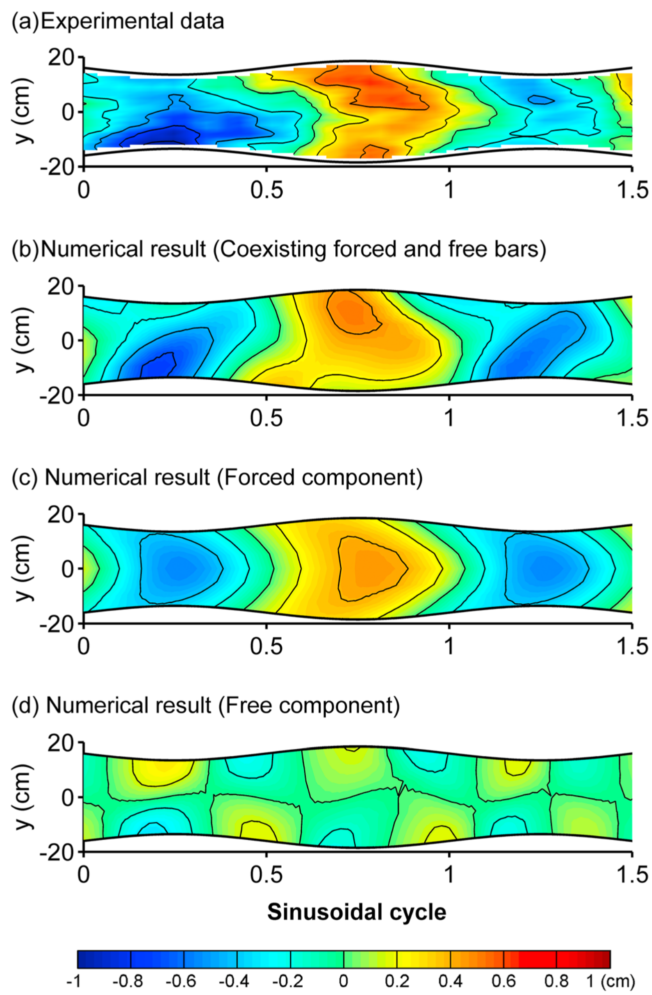

Figure 9. Equilibrium bed deformation in run F-2: (a) Observed distorted central bar [*Wu and Yeh*, 2005]; numerical results (b) coexisting forced and free bars, (c) forced bar and (d) free bar components.

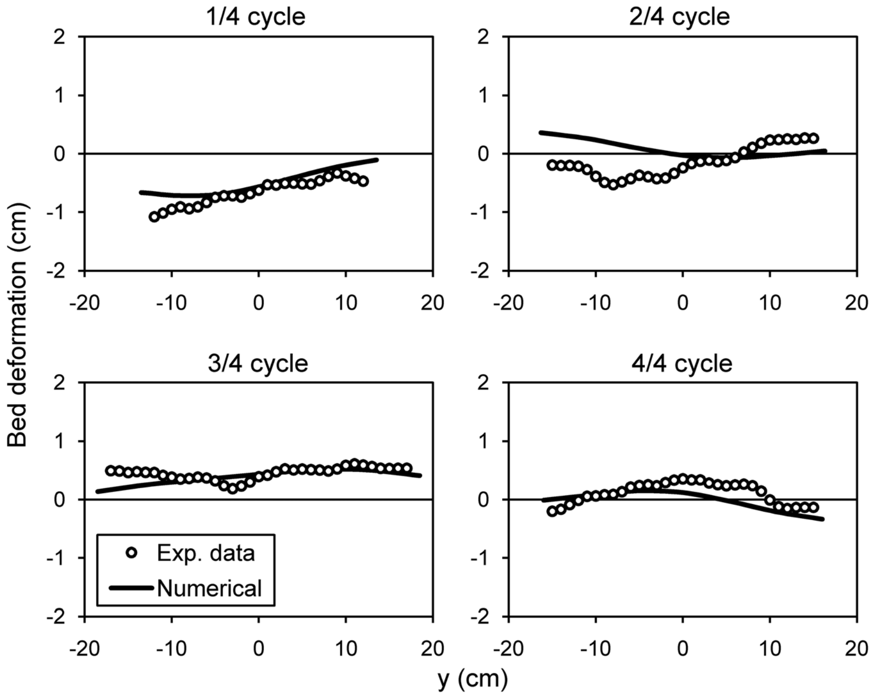

Figure 10. Transverse profiles of equilibrium bed deformation at four cross sections of a sinusoidal cycle (run F-2). The experimental data [*Wu and Yeh*, 2005] and numerical result are shown for a comparison.

in their Case 3 as our base conditions for the reference uniform flow, which include the aspect ratio $\beta = B_0/h_0 = 15$ ($B_0 = 0.15$ m, $h_0 = 0.01$ m), Froude number Fr = 0.8, Shields stress $\theta_0 = 0.07$, unit discharge $q_{in} = 2.5 \times 10^{-3}$ m^2/s, channel slope $S_0 = 0.005$, and sediment size $d_s = 0.43$ mm. These values are adopted here mainly because they allow for fast development of alternate bars, reducing the time needed to reach the equilibrium state. The simulation time of each experiment is 16 h and the length of the channel is 30 m, allowing for four alternate bars fully developed. The channel width is perturbed with different combinations of amplitude and wavelength. A total of 16 combinations are used, composed of four amplitudes A_C = 0.1, 0.2, 0.3, and 0.4 (referred to as A01, A02, A03, and A04 series) and four wave numbers λ_C = 0.2, 0.4, 0.6, and 0.8 (referred to as W02, W04, W06, and W08 series). The values of A_C used in our numerical experiments exceed the limit of small-amplitude assumption, and the values of λ_C used here are beyond the range investigated in earlier studies [*Repetto and Tubino*, 1999; *Repetto*, 2000], thus allowing for a study that covers a broader range of forcing effect. Also, for the parameter values used here, the threshold values of A_C corresponding to the full suppression of bar growth are mostly <0.2, according to the linear stability theory [*Repetto and Tubino*, 1999; *Repetto*, 2000]. As such, more than half of the A_C values used in our numerical experiments exceed the predicted thresholds.

[32] The unit bed load transport rate $q_{b,in} = 1.0 \times 10^{-6}$ m^2/s is evaluated with the given value of θ_0 in the reference uniform flow imposed on the extended reach. An initial bed perturbation is introduced in the upstream extended reach triggering the formation of alternate bars. This bed perturbation is a localized single bump described by (2) with A_b = 3 mm and L_b = 1.6 m, which result in a value of the dimensionless amplitude of bed perturbation A (= A_b/h_0 = 0.3) beyond the small-amplitude regime. This amplitude of bed perturbation, according to *Defina* [2003] and *Bernini et al.* [2006], does not affect the equilibrium bar characteristics but would significantly reduce the time needed to reach an equilibrium state. Prior to the introduction of bed perturbation, the numerical simulation is run for a sufficient time such that the forced bed topography is fully developed in the variable-width channel, as shown in Figure 11, where the equilibrium forced bed forms developed in the 16 variable-width channels studied here are shown. Figure 11 reveals that the bar type (central or two-side bars) is determined by the dimensionless wave number λ_C, whereas the bar amplitude is governed by the dimensionless amplitude A_C. Central bars develop in W02 series ($\lambda_C = 0.2$), while side bars are observed in W04 to W08 series (λ_C = 0.4 to 0.8). Moreover, as A_C increases from 0.1 to 0.4 (A01 to A04 series), the corresponding amplitude of forced bars increases accordingly. The distinct forcing effects associated with the wave number and amplitude of periodic width variations are clearly demonstrated.

[33] Following the introduction of an initial bed disturbance, a train of free bars is developed. These alternate bars superimpose on the existing forced bed forms, resulting in a mixture of bed topographies. The alternate bars subsequently migrate downstream, leaving the forced bed forms undisturbed. An animation is available in the auxiliary material.[1] Shown in Figure 12b are the coexisting free and forced bed forms 8 h after the formation of free bars (A02 series). Subtracting the forced bed forms (Figure 11b) from the mixed bed forms (Figure 12b) gives the free bar components, shown in Figure 12c, where the alternate bars developed in variable-

[1]Auxiliary materials are available in the HTML. doi:10.1029/2010JF001941.

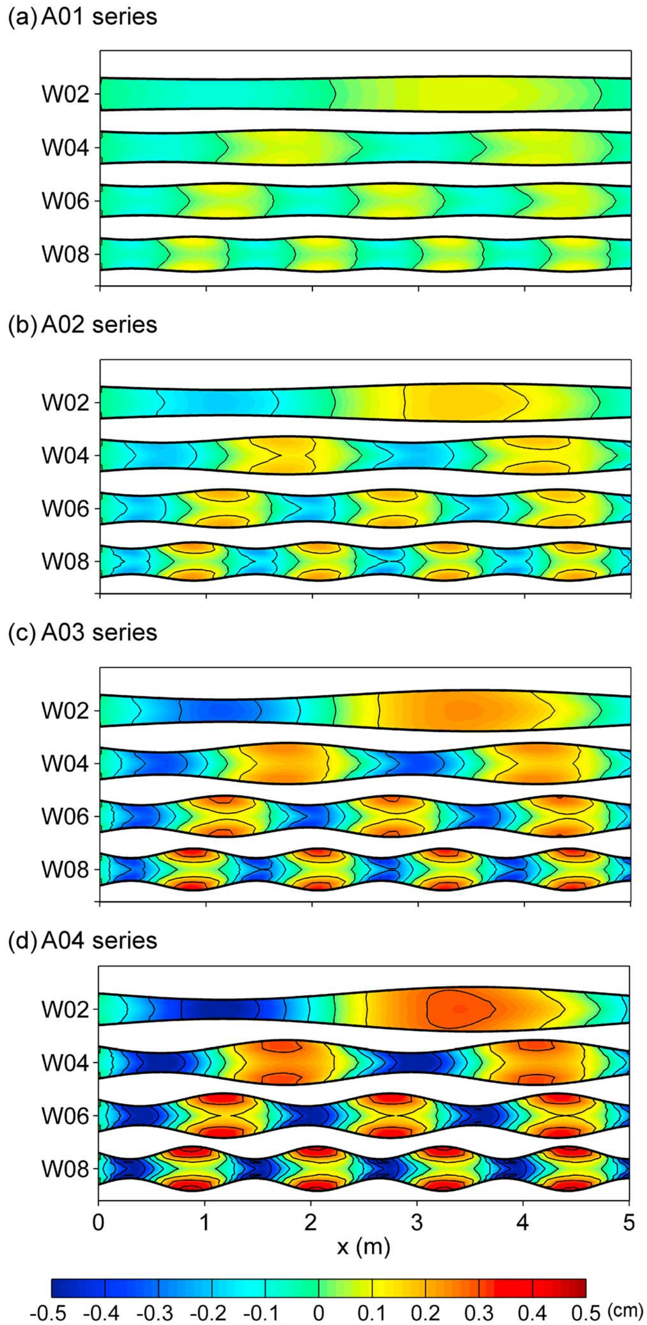

Figure 11. Equilibrium forced bed forms developed in 16 variable-width channels used in numerical experiments. The results reveal that bar type is determined by dimensionless wave number λ_C, whereas bar amplitude is governed by dimensionless amplitude A_C. Central bars are developed in W02 series ($\lambda_C = 0.2$), while side bars are developed in W04 ~ W08 series ($\lambda_C = 0.4 \sim 0.8$). As A_C increases from 0.1 to 0.4 (A01 to A04 series), bar amplitude increases accordingly.

width channels exhibit different degrees of deviation in bar features from the corresponding free bars developed in the reference straight channel (Figure 12a). Such deviations arise from different degrees of forcing effect exerted on the free bars. In subsequent analyses, we will use the equilibrium bar characteristics developed in the straight channel as the base values, and quantify the forcing effect of width variations by comparing the equilibrium bar characteristics developed in the variable-width channels to the straight-channel base values.

4.2. Analysis Procedure

[34] Before we proceed to study the forcing effect of width variations, it is useful to define the terminology used in our analyses. Figure 13 shows the color-scale bed topography and the corresponding longitudinal profile of local bar height 12 h after bar formation in the straight channel, where local bar height is defined as the difference in extreme elevations between the left- and right-half cross section (i.e., difference between red and blue lines). The alternate bars are numbered in a chronicle fashion, i.e., Bar 1 is the one developed immediately downstream of the initial disturbance, Bar 2 is the one immediately downstream of Bar 1, and so forth. The local bar height profile consists of a series of highest and lowest points. Bar length (or wavelength) is defined as the distance between two consecutive lowest points. Keeping track of the location of the highest point allows for the evaluation of bar celerity.

[35] Based on the numerical simulations of 16-h bar evolution in a 30-m channel, we found that the first four

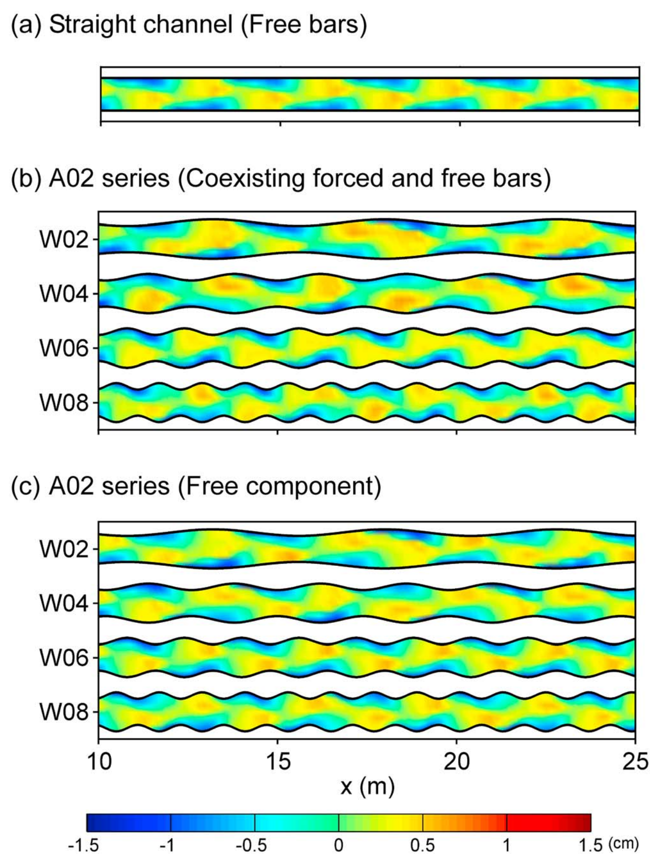

Figure 12. Numerical results: (a) Free bars developed in reference straight channel 8 h after bar initiation; (b) coexisting forced and free bars 8 h after initiation of free bars (A02 series); (c) free bar component extracted from the coexisting bed forms shown in Figure 12b.

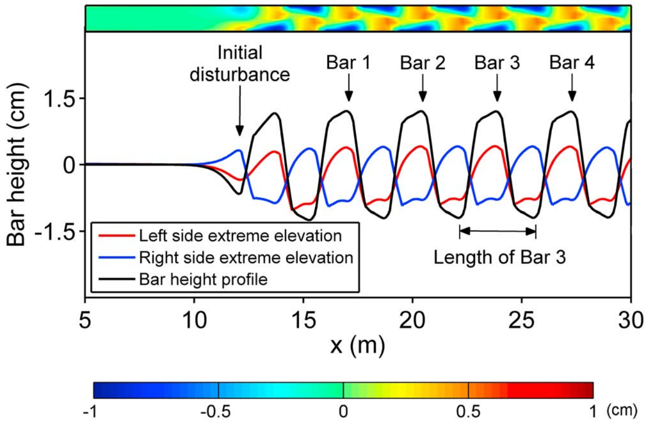

Figure 13. Color-scale bed deformation and the corresponding longitudinal profile of local bar height (difference between red and blue lines) 12 h after bar initiation in the straight channel. Bars are numbered in a chronicle fashion. The bar height profile consists of a series of highest and lowest points. Bar length is defined as the distance between two consecutive lowest points. Keeping track of the location of the highest point allows for evaluation of bar celerity.

bars (hereinafter referred to as target bars) would reach the equilibrium stage for the given time and space frames. Figures 14a and 14b show the evolutions of maximum bar height (B_H), bar length (B_L) and bar celerity (B_C) of the target bars developed in the reference straight channel and A02W04 channel, respectively. These results reveal that as the bar grows, the bar height and length would increase whereas the bar celerity would reduce. Such trends of evolution are first experienced by Bar 1, subsequently by Bar 2 to Bar 4, and all the target bars eventually reach the equilibrium stage after 10 h. The results seen in the straight channel (Figures 14a) are consistent with previous studies [*Defina*, 2003; *Federici and Seminara*, 2003; *Bernini et al.*, 2006]. The results obtained from the variable-width channel (Figure 14b) exhibit similar trends of evolution, however, they also exhibit a wavy pattern associated with periodic variations of local width. The bar height peaks at the narrow sections but troughs at the wide ones, whereas the bar length becomes minimal at the narrow sections but maximal at the wide ones. The celerity reduces at the narrow sections but increases at the wide ones. This adjustment of bar celerity in response to the variation of local width is analogous to the experimental result reported by *Whiting and Dietrich* [1993], where the migrating alternate bars would locally stall when in phase with the curvature-induced point bars in a sinusoidally meandering channel.

[36] To quantify the global effect rather than the local effect of width variations on free bars, the equilibrium features of the target bars in the variable-width channel (Figure 14b) are normalized by the corresponding equilibrium values in the reference straight channel (Figure 14a), resulting in the bar height ratio (R_{BH}), bar length ratio (R_{BL}), and celerity ratio (R_{BC}). These normalized equilibrium bar features represent the relative effects of width variations on free bars, thus may well be used to compare the results obtained from different configurations of width perturbations. Moreover, because all the target bars would not simultaneously reach the equilibrium stage, we implement a shift-and-overlap algorithm to shift in time the normalized features of the target bars to obtain the same overlapping sinusoidal trend at the equilibrium stage. Shown in Figure 15 are the shifted and overlapped bar height ratios (A02W04), where the overlapping

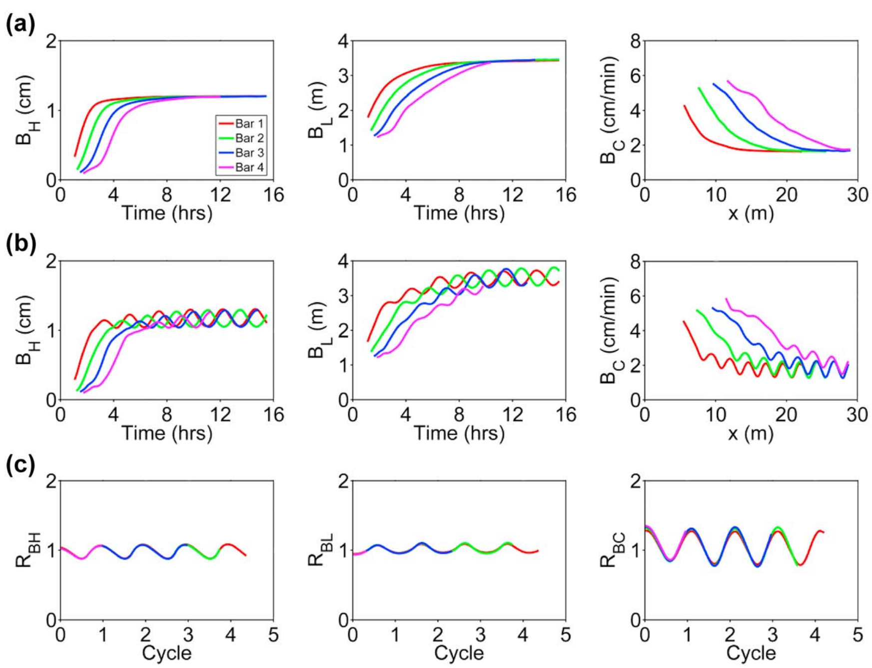

Figure 14. Evolutions of bar height B_H, bar length B_L and celerity B_C of target bars developed in (a) reference straight channel, and (b) A02W04 channel. Data are moving-averaged with 0.5-h windows. (c) Shifted and overlapped equilibrium bar height ratios R_{BH}, bar length ratios R_{BL}, and celerity ratios R_{BC} of target bars.

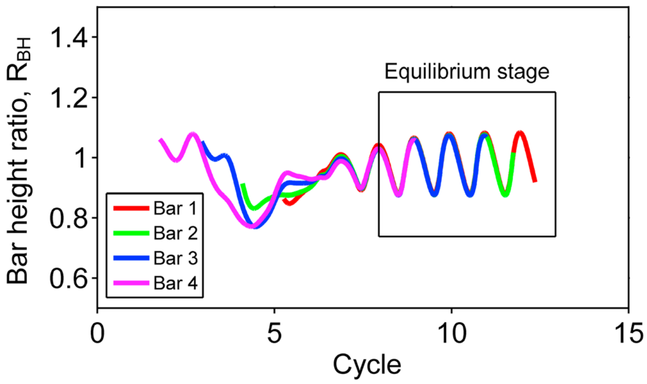

Figure 15. Demonstration of the shift-and-overlap algorithm implemented to shift in time the bar height ratios of target bars to obtain the same overlapping sinusoidal trend at the equilibrium stage (data from run A02W04).

sinusoidal trend at the equilibrium stage and the sequence for the target bars to reach such stage are clearly demonstrated. Note that in Figure 15 the *x*-axis is converted to the number of sinusoidal cycles such that the wavy pattern of equilibrium bar features would echo the periodic width variations.

4.3. Results and Discussion

[37] Shown in Figure 14c are the shifted and matched equilibrium ratios of bar height, bar length, and celerity of the target bars (A02W04), where the overlapping sinusoidal trends of these normalized bar features at the equilibrium stage are clearly demonstrated. The mean values of the sinusoidally varying values of R_{BH}, R_{BL}, and R_{BC} deviate slightly from unity; such deviations represent the global effect of width variations on free bars, whereas the amplitudes of the sinusoidally varying ratios represent the local effect of width variations. The former would be the focus of this study. When the mean value is <1, the global effect of width variations on free bars is suppressive; when the mean value is >1, the global effect is enhancive. For example, in Figure 14c the mean values of R_{BH}, R_{BL}, and R_{BC} are 0.98, 0.99, and 1.02, respectively, indicating that the equilibrium bar height and bar length are reduced while the bar celerity is enhanced relative to the corresponding equilibrium features developed in the reference straight channel.

[38] The forcing effect induced by the sinusoidal width variations turns out to be affected by the amplitude and wave number of width perturbation. Shown in Figure 16 are the equilibrium mean values of R_{BH}, R_{BL}, and R_{BC} varying with the dimensionless amplitude A_C and wave number λ_C of width perturbation. Figure 16a reveals that the equilibrium mean values of R_{BH} are consistently <1, indicating that the global effect of width variations on bar height is invariably suppressive. Such suppressing effect becomes more significant with the increase of A_C and λ_C. However, the effect of A_C is greater than that of λ_C. For example, in Figure 16a (left), the values of R_{BH} reduce with the increase of A_C. For W02 ~ W06 series, the reductions of R_{BH} with the increase of A_C from 0.1 to 0.4 range between 10 ~ 20%, while for W08 series the corresponding reduction of R_{BH} is about 30%. In contrast, in Figure 16a (right), the reductions of R_{BH} with the increase of λ_C from 0.2 to 0.8 are much smaller, especially for A01 and A02 series, for A04 series the corresponding reduction of R_{BH} is higher, however keeping <20%. These results are in part consistent with the theoretical prediction made by *Repetto and Tubino* [1999], who argued that the suppressing effect is governed primarily by the amplitude of width perturbation rather than the wave number. Because this prediction is based on the small-amplitude assumption, it is valid for smaller values of A_C (A01 and A02 series), but would become more ineffective for greater values of A_C (A03 and A04 series).

[39] Similarly, Figure 16b reveals that the suppressing effect of width variations on bar length increases with A_C and λ_C. The reductions of R_{BL} with the increases in A_C and λ_C are of a similar magnitude, but are smaller than the corresponding reductions of R_{BH}. On the other hand, Figure 16c reveals that the global effect of width variations can either reduce or enhance bar celerity, depending on the combination of A_C and λ_C. For example, for W02 and W04 series the equilibrium mean values of R_{BC} are consistently >1, indicating that the global effect on bar celerity is enhancive for smaller values of λ_C. For larger values of λ_C (W06 and W08 series), however, the equilibrium mean values of R_{BC} are >1 for smaller values of A_C but become <1 as the value of A_C exceeds the limit of small-amplitude regime. These results are in agreement with the analytical prediction by *Repetto and Tubino* [1999], who argued that width perturbations in general would slow down bar propagation, but very slow spatial variations of channel width (i.e., very small values of λ_C) would speed up bar propagation. To date this prediction has never been verified with any experimental or numerical data, thus our simulation results are the first evidence available for backing such an argument. Also, it is shown in Figure 16c (left) that for smaller λ_C (W02 and W04 series), the equilibrium mean values of R_{BC} increase with A_C first but then decline as A_C becomes greater than 0.3, while for larger λ_C (W06 and W08 series), the equilibrium mean values of R_{BC} decrease monotonically with the increase of A_C. In Figure 16c (right), the equilibrium means of R_{BC} decline monotonically with the increase of λ_C regardless of A_C. It should be noted here that although the bar celerity is enhanced by smaller values of λ_C, such enhancing effects necessarily vanish for truly small values of λ_C (i.e., as $\lambda_C \to 0$).

[40] The above results indicate that the global forcing effect of width variations may well be quantified using a single factor that integrates the influences of A_C and λ_C. To this end, we define a dimensionless forcing factor F_C, which is expressed as

$$F_C = A_C \exp(\lambda_C) \tag{3}$$

Equation (3) is a modified form of the dimensionless group that incorporates the amplitude and wave number of width variations in the analytical framework of perturbation method [*Wu and Yeh*, 2005]. The use of F_C ensures the collapse of various data on a single curve. We then plot the equilibrium mean values of R_{BH}, R_{BL}, and R_{BC} versus the forcing factor F_C, as shown in Figure 17. The invariably suppressing effects of width variations on bar height and bar length are demonstrated in Figures 17a and 17b, while a slightly enhancing effect on bar celerity followed by suppressing effects at greater values of F_C is demonstrated in Figure 17c. The best fit curves shown in Figures 17a and 17b indicate that while the suppressing effects on bar height and bar length are

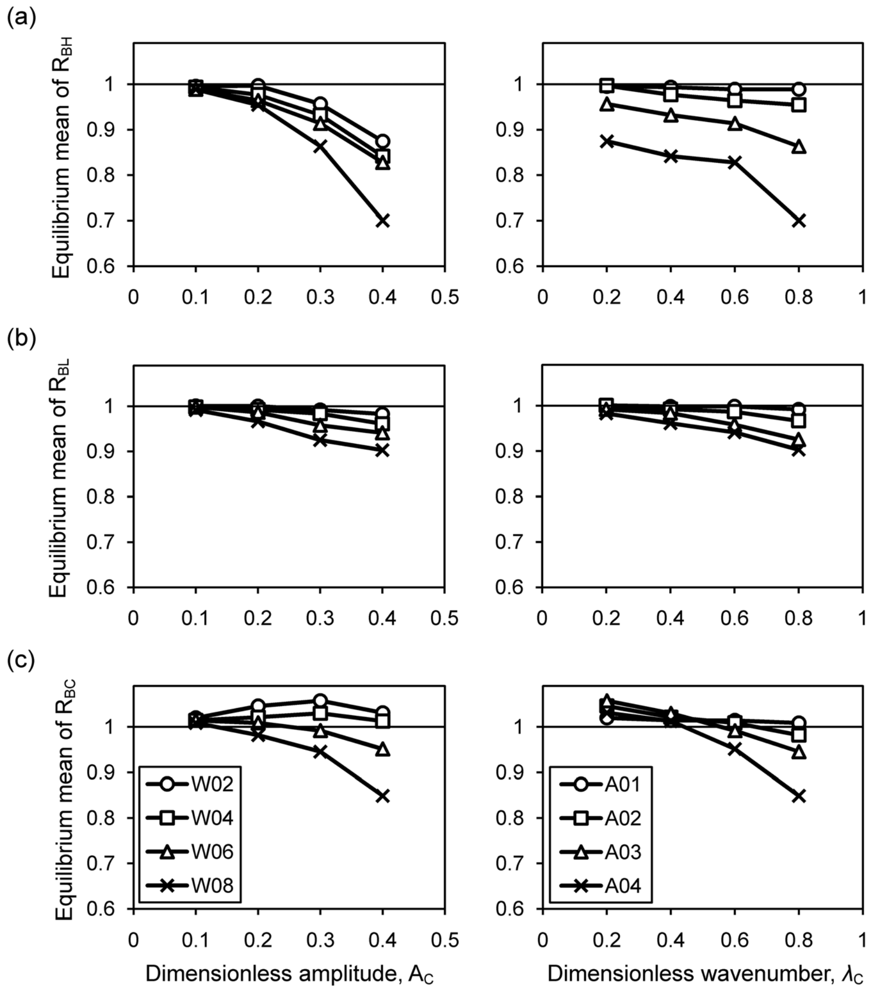

Figure 16. Variations of equilibrium mean values of (a) bar height ratio R_{BH}, (b) bar length ratio R_{BL}, and (c) celerity ratio R_{BC} with (left) dimensionless amplitude A_C and (right) dimensionless wave number λ_C of width perturbations.

both proportional to $F_C^{2.16}$, the effect on bar height is ~3 times that on bar length (i.e., coefficients 0.38 versus 0.13). The best fit curve shown in Figure 17c is quadratic, indicating that bar celerity is slightly increased for $F_C < \sim 0.5$, but is decreased at larger values of F_C. The maximum increase in bar celerity is, however, <5% of the corresponding equilibrium migration speed developed in the reference straight channel.

[41] It is worthwhile to note that, for our experimental ranges of A_C and λ_C, full suppression (or zero growth) of free bars above the threshold A_C, as predicted by *Repetto and Tubino* [1999], is not observed, although most of the A_C values herein used exceed the theoretically predicted thresholds. The discrepancies between the predicted and simulated results may arise from the small-perturbation assumption adopted in the linear stability analysis. Specifically, the adopted dimensionless amplitude of bed perturbation (A = 0.3), as mentioned earlier, is beyond the small-amplitude regime on which the linear stability theory is based. Violation of this assumption on A would make the contribution of the third-order self interactions involving free modes (i.e., $O(A^3)$) become non-negligible, leading to unjustified predictions [*Colombini et al.*, 1987; *Repetto*, 2000]. To address this issue, we tried two additional smaller values of A, 0.03 and 0.003, in a channel with the strongest forcing effect (A04 W08). However, full suppression of free bar growth never took place. Reducing the amplitude of initial bed perturbation would not affect the equilibrium bar features, but would only increase the time needed to reach equilibrium, consistent with the results obtained from the constant-width straight channels [*Federici and Seminara*, 2003]. One possible explanation is that some salient physical process or effect has been poorly treated in the linear analysis, resulting in inaccurate predictions. Nevertheless, our findings that the global suppressing effects on free bars are proportional to $F_C^{2.16}$, i.e., a nearly quadratic function of F_C is, to a certain extent, coherent with the analytical prediction that the damping effects on bar growth and migration speed are proportional to A_C^2 [*Repetto*, 2000].

[42] In any case, an important implication is that the forcing effect of width variations can significantly alter the equilibrium features of free bars. With proper combinations of A_C and λ_C, the migration speed can be increased while the bar height and length can be reduced, which offers a potentially

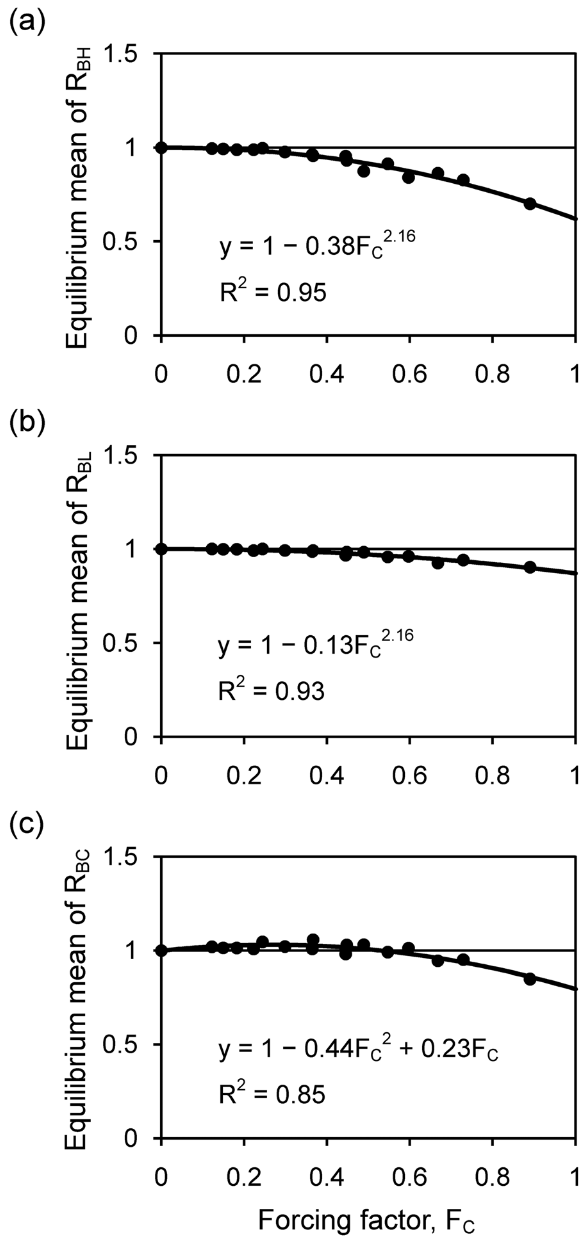

Figure 17. Variations of equilibrium mean value of (a) bar height ratio R_{BH}, (b) bar length ratio R_{BL}, and (c) celerity ratio R_{BC} with dimensionless forcing factor F_C. Effects of A_C and λ_C are integrated in a single factor F_C.

more diversified measure for morphological controls and river management.

5. Conclusions

[43] The forcing effect of channel width variations on free bars is investigated in this study using a 2D depth-averaged morphodynamic model. The novel feature of the model is the incorporation of a CDG scheme in the bed evolution module. A correction for the secondary flows induced by streamline curvature is also included, allowing for simulations of bed form migration in channels with width variations that are beyond small-perturbation regimes. Such correction is particularly important as the small-amplitude assumption for width perturbations is relaxed in our numerical experiments.

[44] Our numerical results provide answers to the questions posed in section 1. For questions (1) and (2): The global effect of width variations on bar height is invariably suppressive. Such suppressing effect increases with the dimensionless amplitude A_C and wave number λ_C of width variations. For values of A_C in the small-amplitude regime, λ_C has little effects on bar height; for values of A_C beyond the small-amplitude regime, however, the suppressing effect is dependent on both A_C and λ_C. Bar length reduction increases also with both A_C and λ_C, but is much weaker than the corresponding effect on bar height. The global effect of width variations can either increase or reduce bar celerity, depending on the combination of A_C and λ_C. For smaller values of λ_C, the effect on bar celerity is enhancive, such enhancing effect, however, would vanish as $\lambda_C \to 0$. For larger values of λ_C, bar celerity tends to increase at small values of A_C, but decreases for A_C beyond the small-amplitude regime. We present in this paper an unprecedented numerical data set that verifies the theoretical prediction on bar celerity enhancement.

[45] For question (3): Regardless of the value of the dimensionless bed perturbation A used, full suppression of bar growth above the threshold A_C, predicted by *Repetto and Tubino* [1999], was not observed in our numerical experiments covering the below- and above-threshold regimes of A_C. Varying the value of A, independently of its small or large amplitude, would not affect the equilibrium bar features, but would only alter the time needed to reach equilibrium. The discrepancy between the analytical prediction and simulation result needs further investigation.

[46] For question (4): The global effects of width variations on free bars can be quantified with a dimensionless forcing factor F_C that integrates the influences of A_C and λ_C. The use of F_C allows the collapse of various data on a single curve. The suppressing effects on bar height and bar length are both proportional to $F_C^{2.16}$; the global effect on bar celerity is a parabolic function of F_C, for $0 < F_C < \sim 0.5$ the celerity is slightly enhanced, while for $F_C > \sim 0.5$ the celerity tends to reduce. These findings are, to some extent, coherent with the previous analytical prediction that the damping effects on bar growth and migration speed are proportional to A_C^2.

[47] As a direction for future studies, the stochastic bed perturbations can be included in the numerical simulations to assess the uncertainty of bar development. Also, a list of complicating factors such as small-scale bed forms, sloping bed, inertial lag, topographic steering, mixed-size sediment, channel curvature, bank erodibility, and floodplain vegetation [*Nelson and Smith*, 1989; *Lanzoni*, 2000b; *Seminara et al.*, 2002; *Defina*, 2003; *Vasquez*, 2005; *Li and Millar*, 2011], may be incorporated into the proposed model to extend its applicability to field-scale problems.

Appendix A: CDG-Based Morphodynamic Model

A1. Hydrodynamic Module

[48] The governing equations of the hydrodynamic module are the depth-averaged 2D Reynolds equations, obtained by vertically integrating the full 3D Reynolds equations over the flow depth [*Steffler and Jin*, 1993; *Molls and Chaudhry*, 1995; *Defina*, 2003]. The resulting system of flow equa-

tions includes a continuity equation and two momentum equations in the x and y (Cartesian planform) directions (for straight channels x and y directions are usually, but not necessarily, taken to be the longitudinal and transverse directions):

$$\frac{\partial h}{\partial t}+\frac{\partial q_x}{\partial x}+\frac{\partial q_y}{\partial y}=0 \tag{A1a}$$

$$\frac{\partial q_x}{\partial t}+\frac{\partial}{\partial x}\left(\frac{q_x^2}{h}+\frac{gh^2}{2}-\frac{T_{xx}h}{\rho}\right)+\frac{\partial}{\partial y}\left(\frac{q_xq_y}{h}-\frac{T_{xy}h}{\rho}\right)+\left(gh\frac{\partial z_b}{\partial x}+\frac{\tau_x}{\rho}\right)=0 \tag{A1b}$$

$$\frac{\partial q_y}{\partial t}+\frac{\partial}{\partial x}\left(\frac{q_xq_y}{h}-\frac{T_{yx}h}{\rho}\right)+\frac{\partial}{\partial y}\left(\frac{q_y^2}{h}+\frac{gh^2}{2}-\frac{T_{yy}h}{\rho}\right)+\left(gh\frac{\partial z_b}{\partial y}+\frac{\tau_y}{\rho}\right)=0 \tag{A1c}$$

where h = flow depth; (q_x, q_y) = unit discharge components in the x- and y-directions = (Uh, Vh), (U, V) = depth-averaged velocity components in the x- and y-directions; t denotes time; g = gravitational acceleration; ρ = density of water; z_b = elevation of bed surface; T_{xx}, T_{yy}, T_{xy}, T_{yx} = depth-averaged Reynolds stresses; (τ_x, τ_y) = x- and y-components of bed shear stress τ, which are evaluated with the classical closure relation:

$$(\tau_x,\tau_y)=(U,V)\rho C_f\sqrt{U^2+V^2} \tag{A2}$$

and

$$C_f=[6+2.5\ln(h/2.5d_s)]^{-2}$$

where C_f = friction coefficient; d_s = sediment size. Note that the correction for the drag due to small-scale bed forms (such as ripples) is not included in (A2) for this study is mainly concerned with large-scale bars. The Reynolds stresses are parameterized using the Boussinesq model:

$$T_{xx}=2\rho\nu_h\frac{\partial U}{\partial x},\, T_{yy}=2\rho\nu_h\frac{\partial V}{\partial y},\, T_{xy}=T_{yx}=\rho\nu_h\left(\frac{\partial U}{\partial y}+\frac{\partial V}{\partial x}\right) \tag{A3}$$

where ν_h = depth-averaged eddy viscosity = 0.5 u_*h [*Ghamry and Steffler*, 2002], and u_* = bed shear velocity = $\sqrt{\tau/\rho}$ = $\sqrt{C_f(U^2+V^2)}$. Note here that the hydrostatic assumption is embodied in (A1), which is valid for most natural channels with small bed slopes. Also, information on the 3D flowfield is lost. Specifically, the effects of topographic steering and secondary flows are not captured by the 2D depth-integrated model [*Olesen*, 1987]. The former is typically weak for long bar wavelengths [*Nelson*, 1990]; while a correction for the effect of secondary flows induced by streamline curvature is incorporated in the direction of bed shear stress (see (A16) for details).

[49] Equations (A1) may be expressed in the matrix form, i.e.,

$$\frac{\partial \boldsymbol{\varphi}}{\partial t}+\frac{\partial \mathbf{f}_x(\boldsymbol{\varphi})}{\partial x}+\frac{\partial \mathbf{f}_y(\boldsymbol{\varphi})}{\partial y}+\mathbf{S}_b(\boldsymbol{\varphi})=0 \tag{A4}$$

and

$$\boldsymbol{\varphi}=\begin{bmatrix}h\\q_x\\q_y\end{bmatrix},\ \mathbf{f}_x(\boldsymbol{\varphi})=\begin{bmatrix}q_x\\ \dfrac{q_x^2}{h}+\dfrac{gh^2}{2}-\dfrac{T_{xx}h}{\rho}\\ \dfrac{q_xq_y}{h}-\dfrac{T_{yx}h}{\rho}\end{bmatrix},$$

$$\mathbf{f}_y(\boldsymbol{\varphi})=\begin{bmatrix}q_y\\ \dfrac{q_xq_y}{h}-\dfrac{T_{xy}h}{\rho}\\ \dfrac{q_y^2}{h}+\dfrac{gh^2}{2}-\dfrac{T_{yy}h}{\rho}\end{bmatrix},\ \mathbf{S}_b(\boldsymbol{\varphi})=\begin{bmatrix}0\\ gh\dfrac{\partial z_b}{\partial x}+\dfrac{\tau_x}{\rho}\\ gh\dfrac{\partial z_b}{\partial y}+\dfrac{\tau_y}{\rho}\end{bmatrix}$$

in which $\boldsymbol{\varphi}$ = solution vector; $\mathbf{f}_x$ and $\mathbf{f}_y$ = flux vectors in the x and y directions, respectively; $\mathbf{S}_b$ = source vector related to the bed characteristics.

[50] For the FE formulation, the solution inside an element is approximated by the nodal values. For the triangular elements, this takes the form

$$\tilde{\boldsymbol{\varphi}}=\boldsymbol{\Phi}\mathbf{B} \tag{A5}$$

and

$$\tilde{\boldsymbol{\varphi}}=\begin{bmatrix}\tilde{h}\\ \tilde{q}_x\\ \tilde{q}_y\end{bmatrix},\ \boldsymbol{\Phi}=\begin{bmatrix}h_1 & h_2 & h_3\\ q_{x,1} & q_{x,2} & q_{x,3}\\ q_{y,1} & q_{y,2} & q_{y,3}\end{bmatrix},\ \mathbf{B}=\begin{bmatrix}B_1\\B_2\\B_3\end{bmatrix}$$

where $\tilde{\boldsymbol{\varphi}}$ = approximate-solution vector; $\boldsymbol{\Phi}$ = nodal-solution matrix, in which h_i, $q_{x,i}$, and $q_{y,i}$ are solutions at node i (for i = 1, 2, 3); $\mathbf{B}$ = vector of local basis functions B_i (also known as shape, trial, or interpolation functions), herein linear Lagrange interpolation functions are used. Replacing the exact-solution vector $\boldsymbol{\varphi}$ with the approximate-solution vector $\tilde{\boldsymbol{\varphi}}$, and applying the Petrov-Galerkin weighted-residual method to (4) leads to

$$\int_\Omega \hat{\mathbf{B}}_i\left[\frac{\partial \tilde{\boldsymbol{\varphi}}}{\partial t}+\frac{\partial \mathbf{f}_x(\tilde{\boldsymbol{\varphi}})}{\partial x}+\frac{\partial \mathbf{f}_y(\tilde{\boldsymbol{\varphi}})}{\partial y}+\mathbf{S}_b(\tilde{\boldsymbol{\varphi}})\right]d\Omega=0,\ \text{for } i=1,2,3 \tag{A6}$$

where Ω = individual element domain; $\hat{\mathbf{B}}_i$ = matrix of weighting (or test) functions for node i. The integration in (6) proceeds on an element-by-element basis. For the CDG scheme [*Hicks and Steffler*, 1992; *Ghanem et al.*, 1995], the weighting-function matrix $\hat{\mathbf{B}}_i$ is given by

$$\hat{\mathbf{B}}_i=\mathbf{B}_i+\mathbf{W}_i=\begin{bmatrix}B_i & 0 & 0\\ 0 & B_i & 0\\ 0 & 0 & B_i\end{bmatrix}+\omega\left(\Delta x\mathbf{W}_x(\tilde{\boldsymbol{\varphi}})\frac{\partial \mathbf{B}_i}{\partial x}+\Delta y\mathbf{W}_y(\tilde{\boldsymbol{\varphi}})\frac{\partial \mathbf{B}_i}{\partial y}\right),\ \text{for } i=1,2,3 \tag{A7}$$

where $\mathbf{B}_i$ = diagonal matrix of B_i; $\mathbf{W}_i$ = upwind matrix for node i; ω = upwinding coefficient ranging between 0.25 ~ 0.75, throughout this study a value of 0.5 is used; Δx and Δy = mean sizes of elements; $\mathbf{W}_x$ $(\tilde{\boldsymbol{\varphi}})$ and $\mathbf{W}_y$ $(\tilde{\boldsymbol{\varphi}})$ = x- and y-components of upwind matrix, which control the distribution (amount and direction) of the numerical dissipation, and are calculated according to (A8) below [*Hughes and Mallet*, 1986], only with $\boldsymbol{\varphi}$ replaced by $\tilde{\boldsymbol{\varphi}}$:

$$\mathbf{W}_x(\boldsymbol{\varphi}) = \mathbf{A}_x\left(\sqrt{\mathbf{A}_x^2 + \mathbf{A}_y^2}\right)^{-1}, \quad \mathbf{W}_y(\boldsymbol{\varphi}) = \mathbf{A}_y\left(\sqrt{\mathbf{A}_x^2 + \mathbf{A}_y^2}\right)^{-1} \tag{A8}$$

where $\mathbf{A}_x$ and $\mathbf{A}_y$ = advection (or convection) matrices in the x and y directions, obtained from the non-conservation form of (A4):

$$\frac{\partial \boldsymbol{\varphi}}{\partial t} + \mathbf{A}_x \frac{\partial \boldsymbol{\varphi}}{\partial x} + \mathbf{A}_y \frac{\partial \boldsymbol{\varphi}}{\partial y} + \mathbf{S}_b(\boldsymbol{\varphi}) = 0 \tag{A9}$$

in which

$$\mathbf{A}_x = \frac{\partial \mathbf{f}_x(\boldsymbol{\varphi})}{\partial \boldsymbol{\varphi}} = \begin{bmatrix} 0 & 1 & 0 \\ gh - U^2 & 2U & 0 \\ -UV & V & U \end{bmatrix}, \quad \mathbf{A}_y = \frac{\partial \mathbf{f}_y(\boldsymbol{\varphi})}{\partial \boldsymbol{\varphi}} = \begin{bmatrix} 0 & 0 & 1 \\ -UV & V & U \\ gh - V^2 & 0 & 2V \end{bmatrix} \tag{A10}$$

The eigenvalues of (A10) are the characteristic velocities of flow disturbances. For example, the eigenvalues of $\mathbf{A}_x$ are U, $U + \sqrt{gh}$, and $U - \sqrt{gh}$, which are the characteristic velocities in the x direction. The inverse matrix $\left(\sqrt{\mathbf{A}_x^2 + \mathbf{A}_y^2}\right)^{-1}$ is calculated using the numerical method suggested by *Hoger and Carlson* [1984].

[51] The quasi-steady approximation of the flowfield permits us to omit the time derivative in (A6). Substituting (A7) into (A6) and integrating (A6) by parts applying the Green's first identity would result in the following weak (or variational) form:

$$\begin{aligned} &\int_\Gamma \mathbf{B}_i\left[\mathbf{f}_x(\tilde{\boldsymbol{\varphi}})\mathrm{n}_x + \mathbf{f}_y(\tilde{\boldsymbol{\varphi}})\mathrm{n}_y\right] d\Gamma \\ &+ \int_\Omega \left[\mathbf{B}_i\mathbf{S}_b(\tilde{\boldsymbol{\varphi}}) - \left(\mathbf{f}_x(\tilde{\boldsymbol{\varphi}})\frac{\partial \mathbf{B}_i}{\partial x} + \mathbf{f}_y(\tilde{\boldsymbol{\varphi}})\frac{\partial \mathbf{B}_i}{\partial y}\right)\right] d\Omega \\ &+ \int_\Omega \left[\omega\left(\Delta x \mathbf{W}_x(\tilde{\boldsymbol{\varphi}})\frac{\partial \mathbf{B}_i}{\partial x} + \Delta y \mathbf{W}_y(\tilde{\boldsymbol{\varphi}})\frac{\partial \mathbf{B}_i}{\partial y}\right)\right] \\ &\cdot \left[\frac{\partial \mathbf{f}_x(\tilde{\boldsymbol{\varphi}})}{\partial x} + \frac{\partial \mathbf{f}_y(\tilde{\boldsymbol{\varphi}})}{\partial y} + \mathbf{S}_b(\tilde{\boldsymbol{\varphi}})\right] d\Omega = 0, \ \text{for } i = 1, 2, 3 \end{aligned} \tag{A11}$$

where Γ = boundary of Ω; (n_x, n_y) = x- and y-components of outward unit normal vector $\mathbf{n}$. The boundary integral term in (A11) represents the natural fluxes across the element boundaries, which provides an accurate and easy means for specifying boundary conditions. For example, for the continuity equation (A1a), the boundary normal flux $q_{\mathbf{n}}$ is given by

$$q_{\mathbf{n}} = \tilde{q}_x \mathrm{n}_x + \tilde{q}_y \mathrm{n}_y \tag{A12}$$

In the system of equations for the entire computational domain, all the inter-element boundary integrals will cancel, thus only the fluxes across the global boundary will remain. For the wall boundaries, $q_{\mathbf{n}}$ is set equal to zero; for the upstream inflow boundary, $q_{\mathbf{n}}$ is a specified unit discharge q_{in}; for the downstream outflow boundary, $q_{\mathbf{n}}$ is treated as an unknown to be solved while a water level needs to be specified.

[52] The Newton-Raphson iterative technique is used to solve the system of equations (A11) for all elements. The iteration procedure is repeated until the error norm of the nodal solutions $\boldsymbol{\Phi}$ becomes smaller than the specified tolerance (10^{-6} is used herein) [*Steffler*, 1997]. The flowfield so obtained is then used in the bed evolution module to calculate the sediment transport rates and, subsequently, the evolution of bed topography, as described below.

A2. Bed Evolution Module

[53] Considering the continuity of sediment associated with bed load transport, the evolution of bed topography may be described by the 2D Exner equation:

$$(1 - \lambda)\frac{\partial z_b}{\partial t} + \frac{\partial q_{b,x}}{\partial x} + \frac{\partial q_{b,y}}{\partial y} = 0 \tag{A13}$$

where z_b = bed elevation; λ = bed porosity (a default value of 0.4 is used); ($q_{b,x}$, $q_{b,y}$) = x- and y-components of bed load transport rate, defined by

$$\left(q_{b,x}, q_{b,y}\right) = q_b(\cos\alpha, \sin\alpha) \tag{A14}$$

where q_b = volumetric bed load transport rate per unit width; α = angle between bed load motion and x-axis. For channels with large-scale bed forms (bars), the bed load angle α is affected by the local bed shear stress and lateral bed slope [*Blondeaux and Seminara*, 1985], as expressed by

$$\sin\alpha = \sin\chi - \frac{r}{\sqrt{\theta}}\frac{\partial z_b}{\partial y} \tag{A15}$$

where χ = angle between local bed shear stress and x-axis; θ = Shields stress = $\tau/(\rho_s - \rho)gd_s$, where $\tau = \rho C_f(U^2 + V^2)$, ρ_s = density of sediment; r = a coefficient ranging between 0.3 ~ 1: a value of 0.3 is used here accounting for the gravitational effect associated with the gently varying transverse bed gradient [*Talmon et al.*, 1995; *Wu and Yeh*, 2005]. For straight channels, where centripetal acceleration is absent, the deviation of the local shear direction from the x-axis is attributed to the effects of depth-averaged transverse velocity and secondary flows induced by streamline curvature (see *Wu and Yeh* [2005] for more details), as expressed by

$$\sin\chi = \frac{V}{\sqrt{U^2 + V^2}} - ahC_s \tag{A16}$$

where a = helical flow coefficient typically ranging between 1 ~ 10 [*Olesen*, 1983], a value of 5 is used here accounting for the streamline convergence and divergence induced by periodic width variations; C_s = local curvature of streamline, determined as follows [*Repetto et al.*, 2002]:

$$C_s = \frac{-\partial(V/U)/\partial x}{\left[1 + (V/U)^2\right]^{3/2}} \tag{A17}$$

Note here that the correction for the inertial adaptation is not included in (A16) or (A17), which is justified for the present study because the phase lag between the bed topography and flowfield is not very significant in straight channels with sinusoidal width variations [*Wu and Yeh*, 2005]. The bed load transport rate q_b is evaluated using the Meyer-Peter and Müller (MPM) formula:

$$q_b = 8(\theta - \theta_c)^{3/2}\sqrt{(\rho_s - \rho)g d_s^3/\rho} \tag{A18}$$

where θ_c = critical Shields stress (= 0.047). As mentioned earlier, the corrections for the effects of longitudinal bed slope and small-scale ripples [*Defina*, 2003] are not incorporated in (A18) because such effects are negligible in the present study.

[54] Applying the Petrov-Galerkin weighted-residual method to (A13) leads to

$$\int_\Omega \left(B_i + W_{b,i}\right)\left[(1-\lambda)\frac{\partial \tilde{z}_b}{\partial t} + \frac{\partial q_{b,x}(\tilde{\varphi})}{\partial x} + \frac{\partial q_{b,y}(\tilde{\varphi})}{\partial y}\right] d\Omega = 0, \quad \text{for } i = 1,2,3 \tag{A19}$$

where $\tilde{z}_b$ = approximate bed elevation in an element = $\sum_{j=1}^{3} B_j z_{b,j}$, $z_{b,j}$ = bed elevation at node j; $W_{b,i}$ = bed-evolution upwind function for node i. For the CDG scheme, $W_{b,i}$ is expressed as

$$W_{b,i} = \omega\left[\Delta x\ W_{b,x}(\tilde{\varphi})\frac{\partial B_i}{\partial x} + \Delta y\ W_{b,y}(\tilde{\varphi})\frac{\partial B_i}{\partial y}\right], \text{for } i = 1,2,3 \tag{A20}$$

where $W_{b,x}$ $(\tilde{\varphi})$ and $W_{b,y}$ $(\tilde{\varphi})$ = x- and y-components of bed-evolution upwind function, given by

$$W_{b,x}(\tilde{\varphi}) = \frac{1-\tilde{\mathrm{Fr}}^2}{\left|1-\tilde{\mathrm{Fr}}^2\right|}\frac{\tilde{q}_x}{\sqrt{\tilde{q}_x^2+\tilde{q}_y^2}}, \quad W_{b,y}(\tilde{\varphi}) = \frac{1-\tilde{\mathrm{Fr}}^2}{\left|1-\tilde{\mathrm{Fr}}^2\right|}\frac{\tilde{q}_y}{\sqrt{\tilde{q}_x^2+\tilde{q}_y^2}} \tag{A21}$$

where $\tilde{\mathrm{Fr}}^2 = (\tilde{q}_x^2 + \tilde{q}_y^2)/g\tilde{h}^3$. Derivation of (A21) is a novel contribution of this study, as given in Appendix B. Similarly, integrating (A19) by parts would lead to the following weak form:

$$\begin{aligned}(1-\lambda)\int_\Omega \left(B_i + W_{b,i}\right)\left(\frac{\partial \tilde{z}_b}{\partial t}\right)d\Omega - \int_\Omega \left[q_{b,x}(\tilde{\varphi})\frac{\partial B_i}{\partial x} + q_{b,y}(\tilde{\varphi})\frac{\partial B_i}{\partial y}\right]d\Omega \\ + \int_\Omega W_{b,i}\left[\frac{\partial q_{b,x}(\tilde{\varphi})}{\partial x} + \frac{\partial q_{b,y}(\tilde{\varphi})}{\partial y}\right]d\Omega \\ + \int_\Gamma B_i\left[q_{b,x}(\tilde{\varphi})\mathrm{n}_x + q_{b,y}(\tilde{\varphi})\mathrm{n}_y\right]\ d\Gamma = 0, \text{for } i = 1,2,3\end{aligned} \tag{A22}$$

in which the boundary integral term can be used to specify bed load fluxes across the boundaries, namely, the boundary normal bed load flux $q_{b,\mathbf{n}} = q_{b,x}(\tilde{\varphi})\mathrm{n}_x + q_{b,y}(\tilde{\varphi})\mathrm{n}_y$. For the wall boundaries, $q_{\mathrm{b},\mathbf{n}}$ is set as zero; for the upstream boundary, $q_{\mathrm{b},\mathbf{n}}$ is a specified bed load transport rate $q_{b,in}$; for the downstream boundary, $q_{\mathrm{b},\mathbf{n}}$ is an unknown to be solved. Using the forward-difference scheme to discretize the time derivative term in (A22) leads to the following explicit form:

$$\begin{aligned}\int_\Omega \left(B_i + W_{b,i}\right)\tilde{z}_b^{t+\Delta t}\ d\Omega = \int_\Omega \left(B_i + W_{b,i}\right)\tilde{z}_b^{t}\ d\Omega + \frac{\Delta t}{(1-\lambda)} \\ \cdot\left\{\int_\Omega \left[q_{b,x}(\tilde{\varphi})\frac{\partial B_i}{\partial x} + q_{b,y}(\tilde{\varphi})\frac{\partial B_i}{\partial y}\right]d\Omega\right. \\ - \int_\Omega W_{b,i}\left[\frac{\partial q_{b,x}(\tilde{\varphi})}{\partial x} + \frac{\partial q_{b,y}(\tilde{\varphi})}{\partial y}\right]d\Omega \\ \left. - \int_\Gamma B_i\left[q_{b,x}(\tilde{\varphi})\mathrm{n}_x + q_{b,y}(\tilde{\varphi})\mathrm{n}_y\right]\ d\Gamma\right\}, \text{for } i = 1,2,3\end{aligned} \tag{A23}$$

where $\tilde{z}_b^{t+\Delta t} = \sum_{j=1}^{3} B_j z_{b,j}^{t+\Delta t}$ = approximate bed elevation inside an element at an advanced time $t + \Delta t$. With the system of equations (A23) obtained for all elements, the nodal values $z_{b,j}^{t+\Delta t}$ over the entire computational domain can be solved. These solutions are then used as the input topographic data to the hydrodynamic module for updating the flowfield.

Appendix B: Upwind Function for Bed Evolution Module

[55] To derive the bed-evolution upwind functions, we must transform the Exner equation into a convective form. We start with the 2D depth-averaged steady flow equations in the channel-fitted coordinate system [*Mosselman*, 1998] such that a streamwise quasi-1D approach can be adopted:

$$\frac{\partial (hU_s)}{\partial s} + \frac{\partial (hU_n)}{\partial n} + \frac{hU_s}{R_n} + \frac{hU_n}{R_s} = 0 \tag{B1}$$

$$U_s\frac{\partial U_s}{\partial s} + U_n\frac{\partial U_s}{\partial n} + g\frac{\partial (z_b + h)}{\partial s} + \frac{U_s U_n}{R_s} - \frac{U_n^2}{R_n} + T_s = 0 \tag{B2}$$

$$U_s\frac{\partial U_n}{\partial s} + U_n\frac{\partial U_n}{\partial n} + g\frac{\partial (z_b + h)}{\partial n} + \frac{U_s U_n}{R_n} - \frac{U_s^2}{R_s} + T_n = 0 \tag{B3}$$

where (s, n) are the streamwise and cross-stream directions, which, in general, do not necessarily coincide with the x and y directions; (U_s, U_n) = s- and n-components of depth-averaged velocity; (R_s, R_n) = radii of curvature of the s- and n-coordinate lines; (T_s, T_n) = s- and n-components of friction term. For a straight or weakly curved channel, both R_s and R_n are much greater than the hydraulic length scales, allowing us to neglect the curvature-related terms. We further resort to the assumption of streamwise quasi-1D flow, i.e., $U_s \gg U_n$ and $U_s^2 \approx U^2 + V^2$, such that the flow equations are reduced to

$$U_s\frac{\partial h}{\partial s} + h\frac{\partial U_s}{\partial s} = 0 \tag{B4}$$

$$U_s\frac{\partial U_s}{\partial s} + g\frac{\partial z_b}{\partial s} + g\frac{\partial h}{\partial s} + T_s = 0 \tag{B5}$$

Substituting (B4) into (B5), and rearranging the resulting equation yields

$$\frac{\partial U_s}{\partial s} = \left(\frac{U_s}{gh - U_s^2}\right)\left(g\frac{\partial z_b}{\partial s} + T_s\right) \tag{B6}$$

The Exner equation in the channel-fitted coordinate system is given by [*Mosselman*, 1998]:

$$(1-\lambda)\frac{\partial z_b}{\partial t} + \frac{\partial q_{b,s}}{\partial s} + \frac{\partial q_{b,n}}{\partial n} + \frac{q_{b,s}}{R_n} + \frac{q_{b,n}}{R_s} = 0 \tag{B7}$$

where $q_{b,s}$ and $q_{b,n}$ = unit bed load transport rates in the streamwise and cross-stream directions. Based on the same assumptions described above, we obtain the quasi-1D form of (B7):

$$(1-\lambda)\frac{\partial z_b}{\partial t} + \frac{\partial q_{b,s}}{\partial s} = 0 \tag{B8}$$

[56] Note that $q_{b,s}$ is a function of bed shear stress, which in turn varies with the flow velocity and depth, as given in (A2). Here we follow *Jansen et al.* [1979] and *Lisle et al.* [2001] to treat C_f as a function of grain size only and neglect the minor influence of flow depth on $q_{b,s}$. Applying the chain rule to (B8), and substituting (B6) into the resulting equation would yield

$$\begin{aligned}\frac{\partial z_b}{\partial t} + \left(\frac{1}{1-\lambda}\right)\frac{\partial q_{b,s}}{\partial U_s}\frac{\partial U_s}{\partial s} &= \frac{\partial z_b}{\partial t} \\ &+ \left[\left(\frac{g}{1-\lambda}\right)\left(\frac{U_s}{gh-U_s^2}\right)\frac{\partial q_{b,s}}{\partial U_s}\right]\frac{\partial z_b}{\partial s} + S = 0\end{aligned} \tag{B9}$$

where

$$S = \left(\frac{1}{1-\lambda}\right)\left(\frac{U_s T_s}{gh-U_s^2}\right)\frac{\partial q_{b,s}}{\partial U_s}$$

Transformation between the channel-fitted and Cartesian coordinate systems gives

$$\frac{\partial z_b}{\partial s} = \frac{\partial z_b}{\partial x}\frac{\partial x}{\partial s} + \frac{\partial z_b}{\partial y}\frac{\partial y}{\partial s} \tag{B10}$$

Substituting (B10) into (B9) leads to

$$\frac{\partial z_b}{\partial t} + C\left(U_s\frac{\partial x}{\partial s}\right)\frac{\partial z_b}{\partial x} + C\left(U_s\frac{\partial y}{\partial s}\right)\frac{\partial z_b}{\partial y} + S = 0 \tag{B11}$$

where

$$C = \left(\frac{g}{1-\lambda}\right)\left(\frac{1}{gh-U_s^2}\right)\frac{\partial q_{b,s}}{\partial U_s}$$

[57] The following relations hold for the streamwise quasi-1D flow:

$$U = U_s\frac{\partial x}{\partial s} \quad V = U_s\frac{\partial y}{\partial s} \tag{B12}$$

[58] Substituting (B12) into (B11) results in

$$\frac{\partial z_b}{\partial t} + CU\frac{\partial z_b}{\partial x} + CV\frac{\partial z_b}{\partial y} + S = 0 \tag{B13}$$

Note that (B13) is a convection form of the Exner equation, analogous to the form given in (A9), indicating that the propagation of bed disturbance is mainly driven by convective flow velocities. The x- and y-components of the bed-evolution upwind function, according to (A8) and (B13), thus take the form

$$\begin{aligned} W_{b,x}(\boldsymbol{\varphi}) &= \frac{CU}{|C|\sqrt{U^2+V^2}} = \frac{1-\mathrm{Fr}^2}{\left|1-\mathrm{Fr}^2\right|}\frac{q_x}{\sqrt{q_x^2+q_y^2}} \\ W_{b,y}(\boldsymbol{\varphi}) &= \frac{CV}{|C|\sqrt{U^2+V^2}} = \frac{1-\mathrm{Fr}^2}{\left|1-\mathrm{Fr}^2\right|}\frac{q_y}{\sqrt{q_x^2+q_y^2}} \end{aligned} \tag{B14}$$

where $\mathrm{Fr}^2 = (U^2 + V^2)/gh \approx U_s^2/gh$ is the Froude number. Equation (B14) indicates that for subcritical flows the upwind function is of the same direction as the convective flow, whereas for supercritical flows the upwind function is of the opposite direction to the convective flow. At last, replacing the nodal values $\boldsymbol{\varphi}$ in (B14) with the approximate solutions $\tilde{\boldsymbol{\varphi}}$ leads to (A21).

Notation

- a helical flow coefficient;
- A dimensionless amplitude of bed perturbation (= A_b/h_0);
- A_b amplitude of bed perturbation;
- A_C dimensionless amplitude of width variations;
- $\mathbf{A}_x$, $\mathbf{A}_y$ advection matrices in the x and y directions;
- $\mathbf{B}$, $\mathbf{B}_i$ vector of B_i, and diagonal matrix of B_i;
- B_C, B_H, B_L bar celerity, maximum bar height, and bar length;
- B_i local basis function;
- $\hat{\mathbf{B}}_i$ matrix of weighting (or test) functions for node i;
- B_0, $B(x)$ mean half-width of the channel, and channel half-width at x;
- C_f friction coefficient;
- C_s local curvature of streamline;
- d_s sediment grain size;
- F_C dimensionless forcing factor = $A_C \exp(\lambda_C)$;
- $\mathbf{f}_x$, $\mathbf{f}_y$ flux vectors in the x and y directions;
- Fr, $\tilde{\mathrm{Fr}}$ Froude numbers corresponding to $\boldsymbol{\varphi}$ and $\tilde{\boldsymbol{\varphi}}$;
- g gravitational acceleration;
- h, h_0 flow depth, and reference uniform flow depth;
- (h_i, $q_{x,i}$, $q_{y,i}$) solutions of flow at node i (for i = 1, 2, 3);
- L_b longitudinal length of bed perturbation;
- L_C wavelength of width variations;
- (n_x, n_y) x- and y-components of outward unit normal vector $\mathbf{n}$;
- q_b, $q_{b,\mathbf{n}}$ bedload transport rate per unit width, and boundary normal bedload flux;
- $q_{b,in}$ unit bedload transport rate from upstream inflow boundary;
- ($q_{b,s}$, $q_{b,n}$) s- and n-components of q_b;
- ($q_{b,x}$, $q_{b,y}$) x- and y-components of q_b;

q_{in}, $q_{\mathbf{n}}$ unit discharge from upstream boundary, and boundary normal flux;
(q_x, q_y) x- and y-components of unit discharge = (Uh, Vh);
r an empirical coefficient for lateral slope (gravitational) effect;
R_{BC}, R_{BH}, R_{BL} ratios of bar celerity, maximum bar height, and bar length;
R_s, R_n radii of curvature of s- and n-coordinate lines;
(s, n) streamwise and cross-stream directions in channel-fitted coordinate system;
$\mathbf{S}_b$ source vector of bed characteristics;
S_0 channel slope;
t time;
T_s, T_n s- and n-components of friction term;
T_{xx}, T_{xy}, T_{yx}, T_{yy} depth-averaged Reynolds stresses;
u_* bed shear velocity;
(U, V), (U_s, U_n) (x, y) and (s, n) components of depth-averaged velocity;
$W_{b,i}$ bed-evolution upwind function for node i;
$W_{b,x}$, $W_{b,y}$ x- and y-components of bed-evolution upwind function;
$\mathbf{W}_i$, $\mathbf{W}_x$, $\mathbf{W}_y$ upwind matrix for node i, and x- and y-components of upwind matrix;
(x, y) Cartesian planform (longitudinal and transverse) coordinates;
z_b, $z_{b,j}$, $\tilde{z}_b$ bed elevation, z_b at node j, and approximate z_b in an element;
α angle between bedload motion and x-axis;
β aspect (width to depth) ratio (= B_0/h_0);
χ angle between local bed shear stress and x-axis;
δz_b bed perturbation;
Δx, Δy mean element sizes;
$\mathbf{\Phi}$ nodal-solution matrix;
Γ boundary of Ω;
$\boldsymbol{\varphi}$, $\tilde{\boldsymbol{\varphi}}$ solution vector, and approximate-solution vector;
λ bed porosity;
λ_C dimensionless wavenumber of width variations (= $2\pi B_0/L_C$);
ν_h depth-averaged eddy viscosity;
θ, θ_c, θ_0 Shields stress, critical Shields stress, and θ of reference uniform flow;
ρ, ρ_s density of water, and density of sediment;
τ, (τ_x, τ_y) bed shear stress, and x- and y-components of τ;
ω upwinding coefficient;
Ω element domain.

[59] **Acknowledgments.** This research was supported by the National Science Council, Taiwan, with the multiyear funds granted to F.-C. Wu (NSC 94-2211-E002-073, 95-2221-E002-256, and 96-2221-E002-233). We thank Jose Vasquez for sharing his modeling experiences with us. We also acknowledge our colleagues at NTU, C. L. Yen, D. L. Young, and H. Capart, for helpful discussions. We appreciate Jon Nelson; two anonymous referees; and the Editor, Michael Church, for thoughtful reviews.

References

Bernini, A., V. Caleffi, and A. Valiani (2006), Numerical modelling of alternate bars in shallow channels, in *Braided Rivers: Process, Deposits, Ecology and Management*, edited by G. H. Sambrook Smith, *Spec. Publ. Int. Assoc. Sedimentol.*, *36*, 153–175.

Bittner, L. D. (1994), River bed response to channel width variation: Theory and experiments, M.S. thesis, Univ. of Ill., Urbana-Champaign.

Blondeaux, P., and G. Seminara (1985), A unified bar-bend theory of river meanders, *J. Fluid Mech.*, *157*, 449–470, doi:10.1017/S0022112085002440.

Bolla Pittaluga, M., B. Federici, R. Repetto, C. Paola, G. Seminara, and M. Tubino (2001), The morphodynamics of braiding rivers: Experimental and theoretical results on unit processes, in *Gravel-Bed Rivers V*, edited by M. P. Mosley, pp. 143–181, N. Z. Hydrol. Soc., Wellington.

Brooks, A. N., and T. J. R. Hughes (1982), Streamline upwind Petrov-Galerkin formulations for convection dominated flows with particular emphasis on the incompressible Navier-Stokes equations, *Comput. Methods Appl. Mech. Eng.*, *32*, 199–259, doi:10.1016/0045-7825(82)90071-8.

Callander, R. A. (1969), Instability and river channels, *J. Fluid Mech.*, *36*, 465–480, doi:10.1017/S0022112069001765.

Chou, Y.-J., and O. B. Fringer (2010), A model for the simulation of coupled flow-bed form evolution in turbulent flows, *J. Geophys. Res.*, *115*, C10041, doi:10.1029/2010JC006103.

Colombini, M., G. Seminara, and M. Tubino (1987), Finite-amplitude alternate bars, *J. Fluid Mech.*, *181*, 213–232, doi:10.1017/S0022112087002064.

Defina, A. (2003), Numerical experiments on bar growth, *Water Resour. Res.*, *39*(4), 1092, doi:10.1029/2002WR001455.

de Vries, M. (1965), Considerations about non-steady bed-load transport in open channels, in *Proceedings of the 11th IAHR Congress*, pp. 381–388, Int. Assoc. for Hydro-Enviorn. Eng. and Res., Delft, Netherlands.

Donea, J., and A. Huerta (2003), *Finite Element Methods for Flow Problems*, Wiley, London, doi:10.1002/0470013826.

Federici, B., and G. Seminara (2003), On the convective nature of bar instability, *J. Fluid Mech.*, *487*, 125–145, doi:10.1017/S0022112003004737.

Fujita, Y., and Y. Muramoto (1982), Experimental studies on stream channel processes in alluvial rivers, *Bull. Disaster Prev. Res. Inst.*, *32*, 46–96.

Fujita, Y., and Y. Muramoto (1985), Studies on the process of development of alternate bars, *Bull. Disaster Prev. Res. Inst.*, *35*, 55–86.

Furbish, D. J., S. D. Thorne, T. C. Byrd, J. Warburton, J. J. Cudney, and R. W. Handel (1998), Irregular bed forms in steep, rough channels 2. Field observations, *Water Resour. Res.*, *34*, 3649–3659, doi:10.1029/98WR02338.

Garcia, M., and Y. Nino (1993), Dynamics of sediment bars in straight and meandering channels: Experiments on the resonance phenomenon, *J. Hydraul. Res.*, *31*, 739–761, doi:10.1080/00221689309498815.

Ghamry, H. K., and P. M. Steffler (2002), Two dimensional vertically averaged and moment equations for rapidly varied flows, *J. Hydraul. Res.*, *40*, 579–587, doi:10.1080/00221680209499902.

Ghanem, A., P. M. Steffler, F. E. Hicks, and N. Katopodis (1995), Two-dimensional finite element modeling of flow in aquatic habitats, *Water Resour. Eng. Rep. 95–S1*, Dep. of Civ. Eng., Univ. of Alberta, Edmonton, Alberta, Canada.

Gill, M. A. (1987), Nonlinear solution for aggradation and degradation channels, *J. Hydraul. Res.*, *25*, 537–547, doi:10.1080/00221688709499254.

Gottlieb, L. (1976), Three-dimensional flow pattern and bed topography in meander channels, *Ser. Pap. 11*, Inst. Hydrodyn. Hydraul. Eng., Tech. Univ. of Denmark, Lyngby.

Hicks, F. E., and P. M. Steffler (1992), Characteristic dissipative Galerkin scheme for open-channel flow, *J. Hydraul. Eng.*, *118*, 337–352, doi:10.1061/(ASCE)0733-9429(1992)118:2(337).

Hicks, F. E., and P. M. Steffler (1995), Comparison of finite element methods for the St. Venant equations, *Int. J. Numer. Methods Fluids*, *20*, 99–113, doi:10.1002/fld.1650200202.

Hoger, A., and D. E. Carlson (1984), Determination of the stretch and rotation in the polar decomposition of the deformation gradient, *Q. Appl. Math.*, *42*, 113–117.

Hughes, T. J. R., and M. Mallet (1986), A new finite element formulation for computational fluid dynamics: III. The generalized streamline operator for multidimensional advective-diffusive systems, *Comput. Methods Appl. Mech. Eng.*, *58*, 305–328, doi:10.1016/0045-7825(86)90152-0.

Ikeda, S., and G. Parker (Eds.) (1989), *River Meandering*, *Water Resour. Monogr. Ser.*, vol. 12, AGU, Washington, D. C.

Jansen, P. P., L. van Bendegom, J. van den Berg, M. de Vries, and A. Zanen (1979), *Principles of River Engineering: The Non-Tidal Alluvial River*, Pitman, London.

Kinoshita, R., and H. Miwa (1974), River channel formation which prevents downstream translation of transverse bars [in Japanese], *Shinsabo*, *94*, 12–17.

Kwan, S. (2009), A two dimensional hydrodynamic river morphology and gravel transport model, M.S. thesis, Univ. of B. C., Vancouver, B. C., Canada.

Lanzoni, S. (2000a), Experiments on bar formation in a straight flume 1. Uniform sediment, *Water Resour. Res.*, *36*, 3337–3349, doi:10.1029/2000WR900160.

Lanzoni, S. (2000b), Experiments on bar formation in a straight flume 2. Graded sediment, *Water Resour. Res.*, *36*, 3351–3363, doi:10.1029/2000WR900161.

Lanzoni, S., and M. Tubino (2000), Experimental observations on bar development in cohesionless channels, *Excerpta*, *14*, 119–152.

Li, S. S., and R. G. Millar (2011), A two-dimensional morphodynamic model of gravel-bed river with floodplain vegetation, *Earth Surf. Processes Landforms*, *36*, 190–202, doi:10.1002/esp.2033.

Lisle, T. E., Y. Cui, G. Parker, J. E. Pizzuto, and A. M. Dodd (2001), The dominance of dispersion in the evolution of bed material waves in gravel-bed rivers, *Earth Surf. Processes Landforms*, *26*, 1409–1420, doi:10.1002/esp.300.

Molls, T., and M. H. Chaudhry (1995), Depth-averaged open-channel flow model, *J. Hydraul. Eng.*, *121*, 453–465, doi:10.1061/(ASCE)0733-9429(1995)121:6(453).

Mosselman, E. (1998), Morphological modelling of rivers with erodible banks, *Hydrol. Processes*, *12*, 1357–1370, doi:10.1002/(SICI)1099-1085(19980630)12:8<1357::AID-HYP619>3.0.CO;2-7.

Nelson, J. M. (1990), The initial instability and finite-amplitude stability of alternate bars in straight channels, *Earth Sci. Rev.*, *29*, 97–115.

Nelson, J. M., and J. D. Smith (1989), Evolution and stability of erodible channel beds, in *River Meandering*, *Water Resour. Monogr. Ser*, vol. 12, edited by S. Ikeda and G. Parker, pp. 321–377, AGU, Washington, D. C.

Oden, J. T., and G. F. Carey (1983), *Finite Elements: Mathematical Aspects*, Prentice-Hall, Englewood, N. J.

Olesen, K. W. (1983), Alternate bars and meandering of alluvial rivers, *Commun. Hydraul. 83–1*, Delft Univ. of Technol., Delft, Netherlands.

Olesen, K. W. (1987), Bed topography in shallow river bends, *Commun. Hydraul. Geotech. Eng., 87–1*, Delft Univ. of Technol., Delft, Netherlands.

Patankar, S. V. (1980), *Numerical Heat Transfer and Fluid Flow*, McGraw-Hill, New York.

Repetto, R. (2000), Unit processes in braided rivers, Ph.D. thesis, Univ. of Genova, Genova, Italy.

Repetto, R., and M. Tubino (1999), Transition from migrating alternate bars to steady central bars in channels with variable width, in *Proceedings of the Internatinal Symposium on River, Coastal and Estuarine Morphodynamics*, vol. 1, 605–614, Int. Assoc. for Hyrdro-Environ. Eng. and Res., Madrid.

Repetto, R., and M. Tubino (2001), Topographic expressions of bars in channels with variable width, *Phys. Chem. Earth, Part B*, *26*, 71–76.

Repetto, R., M. Tubino, and C. Paola (2002), Planimetric instability of channels with variable width, *J. Fluid Mech.*, *457*, 79–109, doi:10.1017/S0022112001007595.

Seminara, G. (2006), Meanders, *J. Fluid Mech.*, *554*, 271–297, doi:10.1017/S0022112006008925.

Seminara, G., and M. Tubino (1989), Alternate bars and meandering: Free, forced and mixed interactions, in *River Meandering*, *Water Resour. Monogr. Ser*, vol. 12, edited by S. Ikeda and G. Parker, pp. 267–320, AGU, Washington, D. C.

Seminara, G., L. Solari, and G. Parker (2002), Bed load at low Shields stress on arbitrarily sloping beds: Failure of the Bagnold hypothesis, *Water Resour. Res.*, *38*(11), 1249, doi:10.1029/2001WR000681.

Shimizu, Y., and T. Itakura (1989), Calculation of bed variation in alluvial channels, *J. Hydraul. Eng.*, *115*, 367–384, doi:10.1061/(ASCE)0733-9429(1989)115:3(367).

Steffler, P. M. (1997), CDG2D Depth Averaged Hydrodynamic Model Reference Manual, report, Civ. Eng. Dep., Univ. of Alberta, Alberta, Edmonton, Canada.

Steffler, P. M., and J. Blackburn (2002), River2D: Two-dimensional depth averaged model of river hydrodynamics and fish habitat, report, Univ. of Alberta, Alberta, Edmonton, Canada.

Steffler, P. M., and Y. C. Jin (1993), Depth averaged and momentum equations for moderately shallow free surface flow, *J. Hydraul. Res.*, *31*, 5–17, doi:10.1080/00221689309498856.

Talmon, A. M., N. Struiksma, and M. C. L. M. van Mierlo (1995), Laboratory measurements of the direction of sediment transport on transverse alluvial-bed slopes, *J. Hydraul. Res.*, *33*, 495–517, doi:10.1080/00221689509498657.

Tubino, M., and G. Seminara (1990), Free-forced interactions in developing meanders and suppression of free bars, *J. Fluid Mech.*, *214*, 131–159, doi:10.1017/S0022112090000088.

Tubino, M., R. Repetto, and G. Zolezzi (1999), Free bars in rivers, *J. Hydraul. Res.*, *37*, 759–775, doi:10.1080/00221689909498510.

Vasquez, J. A. (2005), Two-dimensional finite element river morphology model, Ph.D. thesis, Univ. of B. C., Vancouver, B. C., Canada.

Vasquez, J. A., R. G. Millar, and P. M. Steffler (2007), Two-dimensional finite element river morphology model, *Can. J. Civ. Eng.*, *34*, 752–760, doi:10.1139/l06-170.

Whiting, P. J., and W. E. Dietrich (1993), Experimental constraints on bar migration through bends: Implications for meander wavelength selection, *Water Resour. Res.*, *29*, 1091–1102, doi:10.1029/92WR02356.

Wu, F.-C., and T.-H. Yeh (2005), Forced bars induced by variations of channel width: Implications for incipient bifurcation, *J. Geophys. Res.*, *110*, F02009, doi:10.1029/2004JF000160.

Y.-C. Chen, Y.-C. Shao, and F.-C. Wu, Department of Bioenvironmental Systems Engineering, National Taiwan University, 1, Section 4, Roosevelt Road, Taipei 106, Taiwan. (fcwu@ntu.edu.tw)